University of South-Eastern Norway
Faculty of Technology, Natural Sciences and Maritime Studies

—

Doctoral dissertation no. 116
2022

Zengxing Zhang

Hierarchical Black Silicon and Their Applications

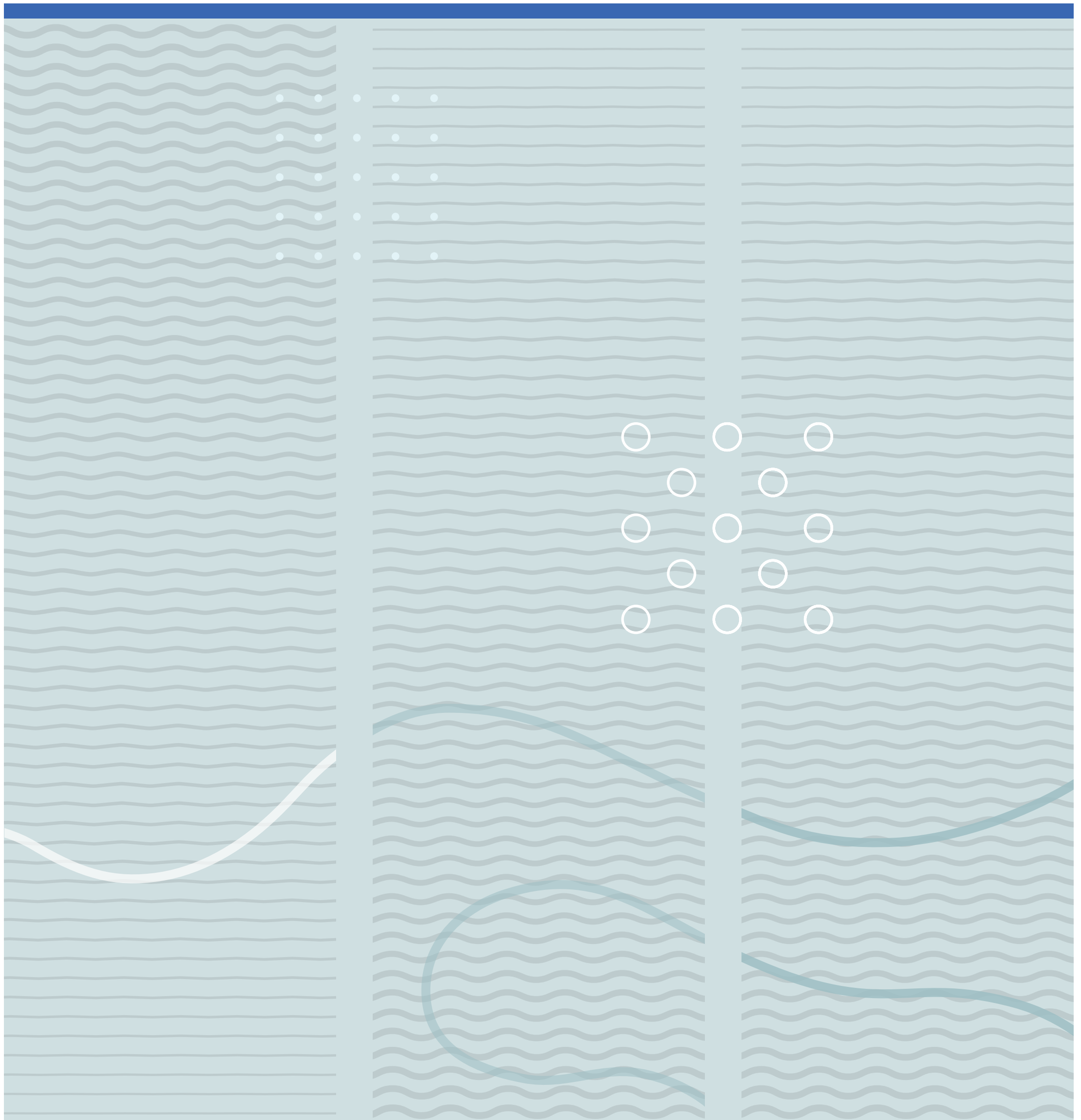

Zengxing Zhang

Hierarchical Black Silicon and Their Applications

A PhD dissertation in
Applied micro- and nanosystems

© Zengxing Zhang, 2022

Faculty of Technology, Natural Sciences and Maritime Studies
University of South-Eastern Norway
Horten, 2022

Doctoral dissertations at the University of South-Eastern Norway no. 116
ISSN 2535-5244 (print)
ISSN 2535-5252 (online)

ISBN 978-82-7206-635-1 (print)
ISBN 978-82-7206-636-8 (online)

This publication is licensed with a Creative Commons license. You may copy and redistribute the material in any medium or format. You must give appropriate credit, provide a link to the license, and indicate if changes were made. Complete license terms at https://creativecommons.org/licenses/by-nc-sa/4.0/deed.en

Print: University of South-Eastern Norway

Preface

This thesis is submitted in partial fulfilment of the requirements for the degree of the Doctor of philosophy (Ph.D.) at the University of South-Eastern Norway (USN). Financial support was supported by the KD program of University of South-Eastern Norway, and the Norwegian Micro- and Nano-Fabrication Facility (NorFab, project number 245963/F50).

The research was conducted from September 2017 to August of 2021 at the Department of Microsystems. Professor Kaiying Wang was the main supervisor, with Professor Frank Karlsen and Professor Henrik Jakobsen as co-supervisors. I would like to thank my supervisors for their guidance, encouragement and support during the past four years. Special thanks to Dr Kang Du and Dr Pai Lu for their enlightening discussions and help to my work. Many thanks to PhD student Avisek Roy, Chaoqun Cheng, Yelzhas Zhaksylyk, Oleksandr Dobroliubov, Chengjun Yu, Fan Chen, Xiao Fan, Kim Robert Gustavsen, Mojde Hasanzade, Yingge Wang, Joseph Joy, Nu Bich Duyen Do, Huyen Thanh Nguyen and Dr Ying Zhao for their continuing friendship.

Appreciations go to the following people for their technical assistance and guidance: Thomas Martinsen, Zekija Ramic, Muhammad Tayyib, Thai Anh Tuan Nguyen and Birgitte Kasin Hønsvall for their professional trainings and help of the experiment set up.

Last but not least, my deepest appreciation and sincere gratitude are extended to my parents, wife and my kids for their unconditional love, understanding and support accompany along with my PhD journey. None of this would be possible without their love and concern.

Zengxing Zhang

September 03, 2021

Abstract

Black silicon is expected to be a promising material for photoelectric, photothermic, photocatalytic, and microfluidic applications due to its remarkably anti-reflectivity, anti-bacterial effect, hydrophilicity, and hydrophobicity. These properties are attributed to the light trapping and surface tension interaction abilities of black silicon surface structures such as pores, pillars, cones, needles, and wires.

Conventional black silicon materials mainly have nanotextures with high aspect ratios and structural density. Nanotextures can be achieved through a series of fabrication approaches, including metal-assisted chemical etching, electrochemical etching, and reactive ion etching (RIE). However, few studies have focused on the surface texturing methodology of black silicon through microstructures.

Anti-reflection is the most critical factor defining the performance of black silicon in optical, photothermic, photochemical, and optoelectronic devices. The properties of these silicon-based devices under visible light illumination are commonly tuned through surface texturing, while their performance at wavelengths higher than 1100 nm requires either intrinsic lattice modification or enhancement by the addition of other materials.

Although a few studies have proposed combining micro and nanostructures, their research has focused on suppressing light reflection at wavelengths lower than 1100 nm. Unfortunately, the anti-reflectance of black silicon in the near-infrared (NIR) range (over 1100 nm) is still weak due to silicon's intrinsic bandgap of 1.12 eV. Fortunately, recent advances in microfabrication and material engineering have enabled the in-depth exploration of the synergy between surface texturing and material reinforcement.

Therefore, building upon innovative fabrication approaches that enable novel black silicon with multi-scale surface structures and the investigation of their optical properties to create new silicon substrate materials for the next generation of photovoltaic, photodetector, and microfluidic devices is the motivation of this work. This Ph.D. work focuses on the following challenges: (1) Development of novel black silicon surface structure designs and relevant fabrication technologies. (2) Investigation

and improvement of the optical properties of novel black silicon through the synergistic effect of surface texture and material reinforcement with localized surface plasmon resonance-inducing Au nanoparticles. (3) Exploration of the potential applications of the as-fabricated black silicon materials.

Keywords: Black silicon, Anti-reflection, Synergistic effect, Hierarchical texture, LSPR, Au nanoparticles, Photothermal generation, Super-hydrophobicity

List of papers

Papers are ommitted from online publication due to publisher's restrictions

Article 1

Z. Zhang et al., “Black silicon with order-disordered structures for enhanced light trapping and photothermic conversion,” Nano Energy, vol. 65, no. June, p. 103992, 2019, doi: 10.1016/j.nanoen.2019.103992

Article 2

Z. Zhang et al., “Ultralow Broadband Reflectivity in Black Silicon via Synergy between Hierarchical Texture and Specific-Size Au Nanoparticles,” Adv. Opt. Mater., vol. 8, no. 19, 2020, doi: 10.1002/adom.202000668

Article 3

Z. Zhang et al., “Fabrication of needle-like silicon nanowires by using a nanoparticles-assisted Bosch process for both high hydrophobicity and anti-reflection,” Micromachines. https://doi.org/10.3390/mi12091009

“Quantum efficiency of UV photodiodes based on black silicon with hierarchical surface textures“. ***(In preparation)***

....

Article 4

Z. Zhang, K. Du, X. Chen, C. Xue, and K. Wang, “An air-cushion triboelectric nanogenerator integrated with stretchable electrode for human-motion energy harvesting and monitoring,” Nano Energy, vol. 53, no. June, pp. 108–115, 2018, doi: 10.1016/j.nanoen.2018.08.011 ***(Not included in this thesis)***

List of figures

Figure 1 Black silicon with nano and micro surface structures: (a) nanopores, (b) nanocones, (c) nanopillars, and (d) microspheres. 1

Figure 2 Overview of the black silicon applications. 4

Figure 3 Super-hydrophobicity caused by black silicon surface texture and chemical treatment.[38] (Left) Cone-like black silicon surface texture. (Right) Needle-like black silicon surface texture. The inset images show hydrophobicity tests using a water droplet. 5

Figure 4 Two black silicon chips bonded together through room-temperature bonding.[38] 6

Figure 5 A comparison between solar cells made using monocrystal silicon and black silicon. (Rasmus Schmidt Davidsen, Technical University of Denmark).. 6

Figure 6 (a) Schematic diagram of near-infrared photodetector based on Schottky barrier and black silicon.[42] (b) Sulphur-doped black silicon-based photodetector.[6] 7

Figure 7 Schematic diagram of the laser irradiation process (a) and the metal-assisted chemical etching process using (b) gold and (c) silver. 10

Figure 8 (a) Oxford Plasma Pro100 instrument. (b) Schematic diagram of basic Bosch etching principles. 11

Figure 9 Schematic diagram of the Bosch etching process. 13

Figure 10 Etching and passivation steps in the Bosch process. (a) Passivation and (b) etching. 14

Figure 11 Relationship between the main parameters of the Bosch process.[56] 15

Figure 12 Schematic diagram of reactive ion etching with a mixture of SF_6 and O_2. 16

Figure 13 (a) Top view and (b) side view SEM images of the achieved needle-like structure obtained via reactive ion etching with a mixture of SF_6 and O_2. 17

Figure 14 The disadvantages of black silicon materials containing only nanostructures. (a) The nanostructure pitch with size below tens to hundreds of nanometers is buried by the deposition of functional materials via (a-1) chemical deposition, (a-2) atom layer deposition, (a-3) sputtering, and (a-4) epitaxial growth. (b) Cell screening by a microfluidic black silicon surface, where (b-1) target cells are unable to be fixed and (b-2) the target cells are easily removed by fluid flow due to the intrinsic small pitch size. (c) The slow desorption of product gas bubbles and the poor wetting contact of the solid interface and reaction liquid, which reduces the reaction speed, as depicted in (c-1) and (c-2). (d) The nanostructured surface is vulnerable to (d-1) friction and (d-2) surface residues, which are difficult to remove............................18

Figure 15 The advantages caused by the introduction of microstructures. (a) Enlarged specific surface area. (b) Creation of protection zone for target cells. (c) Expanded solid-liquid contact area. (d). Hierarchical configuration of micro and nanostructures preventing surface damage. 19

Figure 16 Schematic diagram showing the principle of the two-step etching process to produce a hierarchical texture on a black silicon surface. 21

Figure 17 Honeycomb-like black silicon fabrication schematic diagram. The fabrication consists of two major steps: Bosch etching with a mask to form an ordered micro honeycomb array and RIE with a mixture of SF_6 and O_2 to form disordered nanopores. 22

Figure 18 SEM micrographs of the honeycomb-like black silicon. (a) Tilted view of the honeycomb pores. The inset shows an enlarged view of a sidewall. (b) Top

view of the surface decorated with nanopores. (c) Tilted view of the honeycomb pores decorated with nanopores. (d) Distribution of gold nanoparticles on top of the nanopores. The inset is a digital photograph of the black silicon after gold nanoparticle deposition. 23

Figure 19 Schematic diagram of chimney-like black silicon fabrication process. .. 24

Figure 20 (a) Side view and (b) top view of black silicon with nanopores obtained via RIE with SF_6/O_2, skipping the mask-assisted etching step. (c) Tilted view of textured silicon hollow cylinder array. (d) Tilted view of chimney-like black silicon with hollow cylinders and nanopores. The inset image shows a magnified chimney decorated with nanopores. (e) Digital photograph of textured silicon with a cylinder array. (f) Digital photographs of 4-inch nanopore black silicon wafer (left) and chimney-like black silicon wafer with both a cylinder array and nanopores (right)... 25

Figure 21 SEM images showing tilted views of silicon surfaces with only hollow cylinder arrays (upper images) and chimney-like black silicon surfaces with both hollow cylinders and nanopores (lower images). (a) SEM images of samples with cylinder diameters of 10 µm and a pitch of 2 µm. (b) SEM images of samples with cylinder diameters of 8 µm and a pitch of 4 µm. (c) SEM images of samples with cylinder diameters of 8 µm a pitch of 2 µm, and heights of 31 µm.. 26

Figure 22 The scheme for the fabrication of the Nanowire black silicon. The fabrication process consists of gold sputtering and annealing to form a gold particle mask, followed by three etching steps: an initial Bosch etching, undercut etching, and further etching to remove the gold nanoparticles. ... 27

Figure 23 SEM images of nanowire black silicon fabricated via modified Bosch process. (a) Tilted view of the nanoparticle mask on the top of the nanowires. (b) Tilted view of the silicon nanowires. (c) Top view of the silicon nanowires. (d) Tilted view of the silicon nanowires at a lower magnification. 29

Figure 24 Photographs of the nanowire black silicon in pieces (left) and wafer level (right) formed by using a 4 nm gold nanoparticle mask and 120 etching loops. 30

Figure 25 Tilted and top view SEM images of nanowire black silicon obtained by using (a) gold nanoparticle mask formed by 4 nm gold film and 160 etching loops, (b) gold nanoparticle mask formed by 6 nm gold film and 160 etching loops, (c) gold nanoparticle mask formed by 8 nm gold film and 160 etching loops, and (d) gold nanoparticle mask formed by 10 nm gold film and 160 etching loops. 31

Figure 26 Digital photographs of the nanowire black silicon formed through 160 etching loops. The nanoparticle masks are formed by 4, 6, 8, and 10 nm Au films, respectively. 32

Figure 27 Reflection and transmission of light on a textured silicon substrate. 34

Figure 28 Schematic diagram of the anti-reflective principle of optical waves propagating through surfaces with different structural features: (a) flat surface, (b) surface with nanopores, (c) surface with micropores, and (d) surface with micro-nanopores. 35

Figure 29 Optical measurements on silicon with different aperture to spacing ratios and etching processes. (a) The reflectance of planar silicon and honeycomb-like silicon with ordered micropores. (b) The transmittance of planar silicon and honeycomb-like silicon with ordered micropores. (c) The reflectance of silicon before and after different etching treatment steps. (d) The transmittance of silicon with different etching treatment steps. Ordered micropore sample Si-4 is chosen for the comparison tests in (c) and (d). 36

Figure 30 Digital photograph of a black silicon wafer in which the square areas contain hierarchical textures consisting of honeycomb-like micropores and

decorated nanopores. In contrast, the remaining area contains only nanopores. 37

Figure 31 (a) Light trapping mechanism in black silicon with hierarchical texture. (b) Schematic diagram showing the dominant light absorption mechanism in Au NPs smaller than 50 nm. (c) Anti-reflection due to synergy between Au NP-induced LSPR and hierarchical texture of black silicon surface. 38

Figure 32 (a) Side view of the hierarchical chimney-like silicon structure decorated with Au NPs. The scale bar is 5 µm. (b) Magnified view of Au NPs at four selected positions on the hierarchal chimney-like silicon surface. All scale bars are 100 nm. (c) Measured reflectance spectra of the nanopore and hierarchical textured black silicon surfaces. Both structures are decorated with Au NPs formed from a 4 nm Au film. The inset shows a magnified view of the measured spectra from the hierarchical surface. (d) Measured transmittance spectra of the nanopore and hierarchical textured surface. Both are decorated with Au NPs formed from a 4 nm Au film. 41

Figure 33 (a) Measured reflectance spectra of the hierarchical chimney-like black silicon decorated with nanoparticles formed from Au films with varying thickness. (b) Measured reflectance spectra of different hierarchical surface structures, all of which have the same nanopore decoration and Au NPs formed from a 4 nm gold film. 42

Figure 34 (a) Testing platform for steam generation. The inset photo shows the thermocouple detecting head immersed in water and bubble growth on the sample surface. (b) Change in the mass of water with time under 4 kW m^{-2} solar irradiation. (c) Water temperature vs. time. (d) Testing platform for photo-thermal-electric experiment. A LabVIEW program was used to record real-time output. (e) The black silicon, generator, and cooling fin are fixed together using thermally conductive silicone and the aluminium fins are immersed in an ice-water mixture. (f) The output voltages of the

thermoelectric generator vs. time. *Note: the order-disordered Si has honeycomb-like micropores and nanopores on its surface, and the disordered nanopore Si only has nanopores on its surface.* 43

Figure 35 Contact angles of water droplets on nanowire black silicon surfaces formed through (a) 160 and (b) 180 etching loops. (c) Images of a 1.5 µL water droplet dropped onto a silicon nanowire surface bouncing ten times. The video framerate represents 4000 frames per second..................................46

Figure 36 Black-Silicon Ultraviolet Photodiodes designed by researchers at Aalto University [70]. (a) A schematic diagram of photodiodes and quantum efficiency at wavelengths of 200 to 800 nm. SEM images of device structures. (b) and (c) Bird's eye view SEM image of b-Si nanotexture with cone-like and columnar-like morphologies, respectively...51

Figure 37 Cross-sectional view of our photodiode on the black silicon with hierarchical surface texture. (Unpublished) 51

Figure 38 The working principle of the black silicon-based ultraviolet photodiode. (Unpublished)..52

Figure 39 Fabrication process of ultraviolet photodiode on the black silicon with hierarchical surface texture. (Unpublished) 53

Figure 40 Digital photograph of black silicon ultraviolet photodiode on a 4-inch wafer. (Unpublished) 54

Figure 41 Testing platform. (Unpublished)..55

Abbreviations

RIE	*Reaction ion etching*
NIR	*Near-infrared*
NPs	*Nano particles*
LSPR	*Localized surface plasmon resonance*
DRIE	*Deep reactive ion etching*
ICP	*Inductively coupled plasma etching*
MACE	*Metal assisted chemical etching*
RF	*Radio frequency*
SEM	*Scanning electron micrographs*
EDX	*Electron dispersion or energy dispersive X-ray spectroscopy*
TEM	*Transmission electron microscopy*
XPS	*X-ray photoelectron spectroscopy*
Ti	*Titanium*
TiO_2	*Titanium Dioxide*
DI	*Deionized*
HF	*Hydrogen Fluoride*
SF_6	*Sulfur hexafluoride*
C_4F_8	*Tetrafluoride*
O_2	*Oxygen*
NPs	*Nanoparticles*
Au	*Gold*
Ag	*Silver*
Al_2O_3	*Aluminium oxide*
CHF_3	*Trifluoromethane*
C_3F_8	*Octafluoropropane*
C_4F_8	*Octafluorocyclobutane*
SiF_4	*Silicon tetrafluoride*
e^-	*Electron*
F^*	*Fluorine ion*

Table of contents

1 Black silicon **1**

1.1 Introduction to black silicon 1

1.2 Application of black silicon 4

2 Black silicon fabricated via reactive ion etching **9**

2.1 Bosch etching process 11

2.2 Reactive ion etching using SF_6 and O_2 mixture 16

2.3 Inspiration 18

3 Novel black silicon fabricated via two-step reactive ion etching **22**

3.1 Honeycomb-like black silicon 22

3.2 Chimney-like black silicon 24

3.3 Nanowire black silicon 27

4 Light trapping and application of novel black silicon **33**

4.1 Light trapping definition 33

4.2 Light trapping on hierarchical surface texture 34

4.3 Light trapping via synergistic effect of hierarchical surface texture and LSPR particles with specific size 37

4.4 Photo-thermal-electric generation 43

4.5 Super-hydrophobicity on nanowire black silicon 46

5 Conclusions and future prospects **48**

5.1 Conclusion 48

5.2 Future application 49

5.2.1 Black-Silicon Ultraviolet Photodiodes with External Quantum Efficiency above 130% 50

5.2.2 Principle of black-silicon ultraviolet photodiodes 51

5.2.3 Fabrication process of Ultraviolet Photodiode on black silicon with hierarchical surface texture 53

5.2.4 Future work 55

6 References **56**

7 Articles ....

Articles are ommitted from online publication due to publisher's restrictions

1 Black silicon

1.1 Introduction to black silicon

As one of the most earth-abundant elements, silicon is widely used in photodetectors, optical communications, and microelectronics. Silicon is the dominant raw material used in microelectronic devices[1]–[3]. However, the reflectivity of crystalline silicon to visible and infrared light is so high that it diminishes the key technical indicators of silicon-based devices such as sensitivity, available spectrum range, and conversion efficiency[4]. In recent years, silicon materials with anti-reflective surface textures have attracted significant attention. Typically known as black silicon[1], [5]–[7], these materials have a black surface formed by structures such as pores, wires, pillars, and spheres at the micro and nanoscale, as illustrated in Figure 1(a), (b), (c), and (d). These textures are classified by geometry as ordered/disordered and by size as micro/nano. High aspect ratios, structural density, and wavelength-matched surface structures lead to excellent anti-reflective ability[6]. These textures extend the optical path length of incident light and allow more light energy decay through the coupling effect between light and silicon. The behaviour traps light in these micro and nanostructures leading to light energy decay, referred to as the light-trapping effect[8], [9]. This light-trapping effect allows the easy implementation of black silicon with low reflection in the visible range.

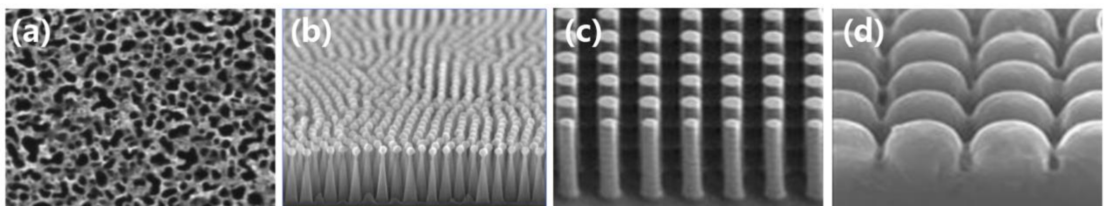

Figure 1 Black silicon with nano and micro surface structures: (a) nanopores, (b) nanocones, (c) nanopillars, and (d) microspheres.

To date, the black silicon with high aspect ratio surface nanostructures exhibits the highest light-trapping capabilities. For instance, nanowires and nanopillars offer extended light path lengths and smaller feature sizes[9]. These nanostructures have

ordered and disordered arrangements[10]–[13] and have shown merit in subsequent material engineering processes. Black silicon with ordered surface structures has homogeneous structural features such as diameter, length, alignment, and inter-spacing. Such black silicon exhibits smooth surfaces, consistent performance and is under controllable fabrication. Black silicon with disordered textures yields high aspect ratio features but limited inter-space, inhomogeneity, and a higher number of recombination defects. Optical or electron beam lithography are suitable approaches for obtaining the required patterns for black silicon with ordered surface texture. However, the limitations of lithography mask resolution limit the scale and manufacturing of ordered nanostructures. Furthermore, subsequent material engineering for specific applications faces several challenges, such as reduced light anti-reflectivity, more defects, and weak self-cleaning ability[14]. Compared to the conventional nanostructures of black silicon, microscale surface textures have larger feature sizes and quickly form ordered arrays with straight pores and adequate space[11], [12], [15]. Microscale ordered structures also have large dimensional variation that allows for the fabrication of complex three-dimensional (3D) devices. In addition to these benefits, microscale textures are subject to the drawbacks of low structural density, aspect ratio, and surface area. Therefore, it is still a challenge to create black silicon with superior anti-reflection textures at either the micro or nanoscale.

Reported approaches for fabricating black silicon include femtosecond laser pulsing[16], [17], reaction ion etching (RIE)[18], electrochemical corrosion[19], [20], and metal-assisted chemical etching[21], [22]. Dry etching methods such as RIE have the advantages of high anisotropy and high-precision patterning. RIE offers highly anisotropic etching and creates vertical sidewalls with smooth surfaces. Usually, RIE methods used in black silicon fabrication are classified as mask-assisted or maskless etching[23]. Mask-assisted RIE create surface textures at both the micro and nanoscale while maskless RIE only create nanostructures. In addition to surface texturing, material engineering has expanded black silicon's functionality[24]–[29]. For example, ion implantation increases charge carrier density, dual-layer passivation reduces photogenerated charge recombination, induced junctions enhance quantum efficiency,

and noble metal nanoparticles can be deposited to generate a plasmon resonance effect[30]. As a result, black silicon has been utilized in a versatile range of optoelectronic, photovoltaic, photo-thermal-electric, and photochemical applications. Overall, light conversion on black silicon relies on two basic mechanisms: photoelectric and photothermic effects. In either case, the initial light anti-reflectivity of black silicon determines the light conversion efficiency, indicating that novel surface structures and material modification methods are required to maximize black silicon's light-trapping and energy converting abilities.

The anti-reflectance of silicon in the near-infrared (NIR) range at wavelengths over 1100 nm is weak because it is challenging to break through silicon’s intrinsic bandgap of 1.12 eV[1], [6], [7], [25]. Femtosecond-laser processing dopes sulphur and oxygen into silicon as impurities to reduce the bandgap. These impurities allow electrons to cross the bandgap under the activation of two near-infrared photons, leading to high near-infrared light absorption. However, impurity distribution rates and content are difficult to control. Impurity doping is susceptible to thermal annealing and has a high cost. Another silicon modification method is metallic nanoparticle (NP) deposition to confine the charge density oscillations and induce localized surface plasmon resonance (LSPR). Smaller NPs exhibit electromagnetic field enhancement under electromagnetic wave excitation, while light scattering dominates the optical response of larger NPs. Both of these effects contribute to the improvement of black silicon anti-reflection properties. LSPR effects concerning noble metal, alloy, structured, and mixed NPs have also been applied to conventional anti-reflective surfaces. This technique has been highly successful for improving the overall anti-reflection performance of black silicon and the conversion efficiency of photoelectronic devices.

A few studies have so far proposed combining micro- with nanostructures but mainly focus on suppression of light reflection at wavelengths below 1100 nm [31]–[36]. On the other hand, the combination of hierarchical surface texture containing micro- and nanostructures could overcome the broadband reflection challenge in black silicon via the decoration of absorption-dominant particles produced by specific LSPR particles.

Therefore, the present thesis focuses on the fabrication of novel black silicon with hierarchical surface structures, as well as exploring a novel LSPR particle decoration approach to create a synergistic light extinction effect.

1.2 Application of black silicon

The micro and nanoscale surface protrusions in black silicon led to desirable properties, such as low reflectivity, super-hydrophobicity, and terahertz wave generation. These properties are suitable for various applications in engineering fields. Figure 2 summarizes the current applications of black silicon. For example, the low reflectivity of black silicon and high absorption of visible light are great features to promote the performance of solar cells. The use of black silicon as photoelectric catalytic substrates may synergize light absorption and redox catalysts to improve the catalytic rates. Also, the excellent light absorption capability of black silicon-based photodetectors in the visible and near-infrared bands would yield high sensitivity surface-enhanced Raman scattering (SERS)[37]. In the following paragraphs, five applications of black silicon are described.

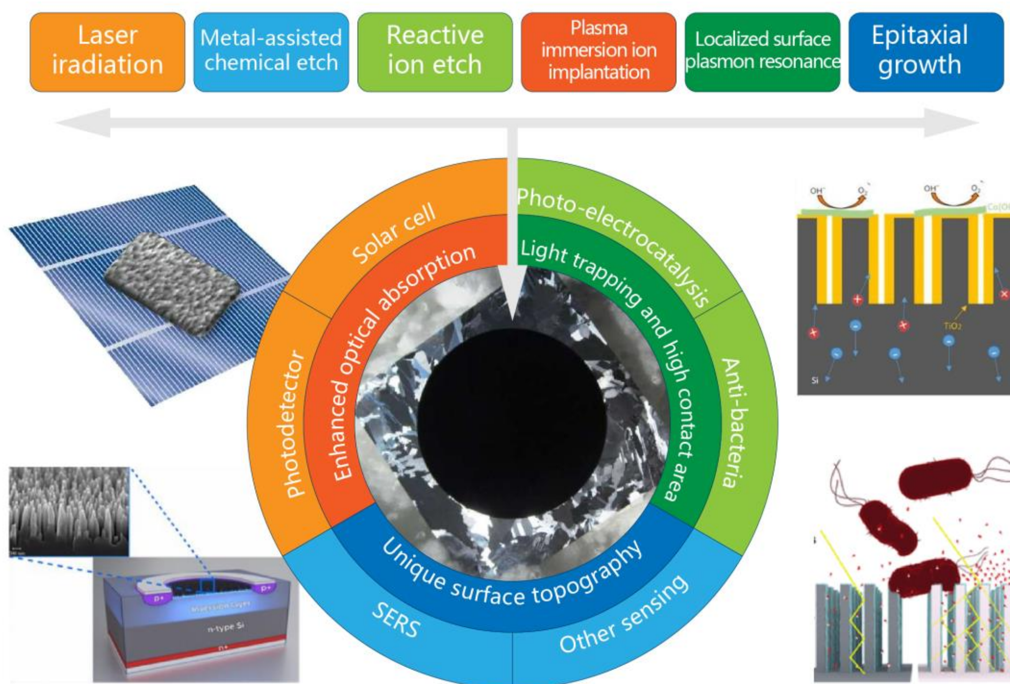

Figure 2 Overview of the black silicon applications.

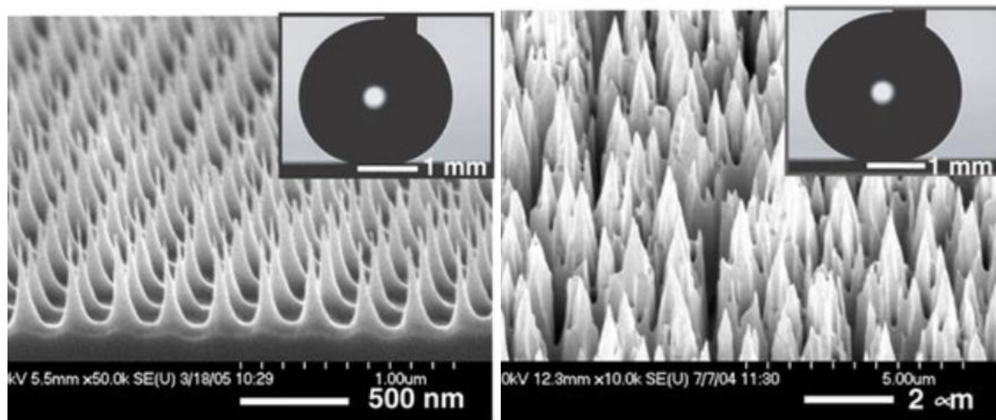

Figure 3 Super-hydrophobicity caused by black silicon surface texture and chemical treatment.[38] (Left) Cone-like black silicon surface texture. (Right) Needle-like black silicon surface texture. The inset images show hydrophobicity tests using a water droplet.

Black silicon with high-density surface structures, such as wires, needles, and sharp cones exhibit excellent hydrophobicity, known as super-hydrophobicity. It is worth noting that super-hydrophobicity means that water droplets have minimal contact with the surface texture of black silicon under the action of surface tension[39]. Meanwhile, hydrophobic surfaces generally refer to surfaces with water contact angles larger than 90°. Surfaces with water contact angles larger than 150° are referred to as superhydrophobic surfaces[39]. After deposition of a hydrophobic polymer, black silicon surface textures yield static contact angles higher than 150° with pure water droplets. In nature, lotus leaves have similar surface textures allowing water droplets to flow and remove dust, resulting in a self-cleaning functionality. Super-hydrophobicity could also be applied in the design of microelectromechanical system microfluidic channels to reduce liquid friction in flow channels. Figure 3 shows the superhydrophobic properties of black silicon surface textures after chemical treatment. Both the black silicon with cone-like (Left) and needle-like (Right) surface textures have hydrophobic behaviours. The insets illustrate the apparent contact angles of water droplets after the application of a hydrophobic Teflon coating on each surface.

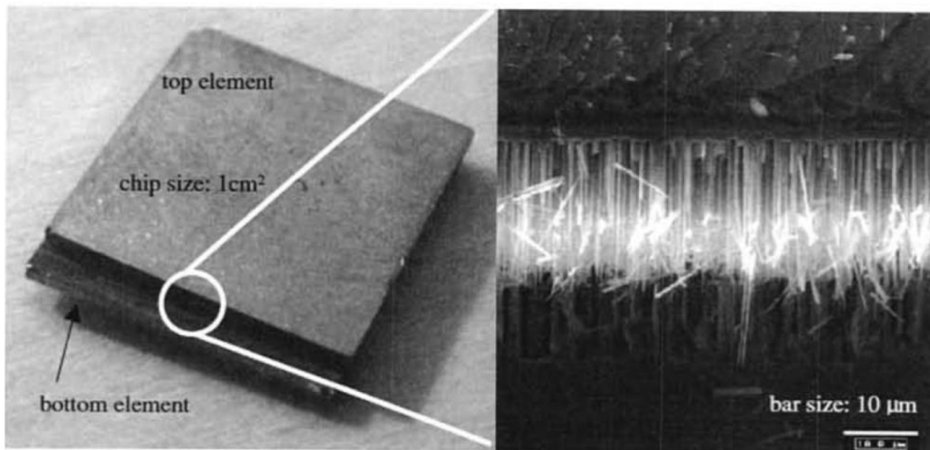

Figure 4 Two black silicon chips bonded together through room-temperature bonding.[38]

Needle-like black silicon structures have been used in room-temperature bonding processes. Generally, bonding requires immense pressure and high temperature. In contrast, the needle-like structures on a black silicon material surface interlock like two brushes pushed together due to their close arrangement. As shown in Figure 4, two silicon wafers with the same black silicon structure are tightly bonded together at room temperature.[38]

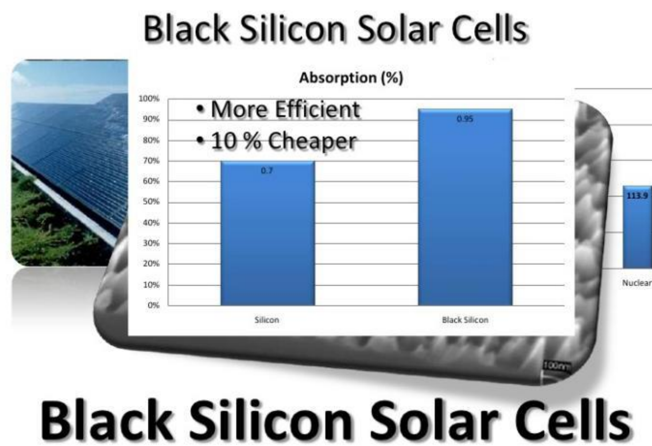

Figure 5 A comparison between solar cells made using monocrystal silicon and black silicon. (Rasmus Schmidt Davidsen, Technical University of Denmark)

The superior anti-reflectivity of black silicon is of great interest for many applications. Its reflectivity in the ultraviolet and visible light regions is lower than 2%, and a recently developed black silicon material has shown a reflectivity lower than 5% in the near-

infrared range. In comparison, the reflectivity of a typical polished monocrystalline silicon wafer exceeds 30%. Figure 5 shows a light absorption comparison between solar cells made of monocrystal silicon and black silicon[40]. Statistics show that black silicon solar cells have more efficient absorption and are 10% much cheaper than conventional silicon solar cells, owing to the excellent low reflectivity caused by the surface textures. The extremely low reflectivity of black silicon has aroused researcher interest for photovoltaic applications. Many studies have been reported that utilize the excellent anti-reflectivity of black silicon to increase the efficiency of solar energy harvesting. Solar cell efficiency with black silicon substrates has been increased from 13.7% to 16.8%. Some companies have fabricated mass-produced solar cells with an efficiency of 17%.

Black silicon also shows significant potential for generating terahertz waves[41]. Although terahertz waves are widely used in the communication, medical, security, and military fields, one obstacle to their practical application is the difficulty in generating terahertz waves. The successful development of black silicon for terahertz wave generation is expected to significantly promote these field's development.

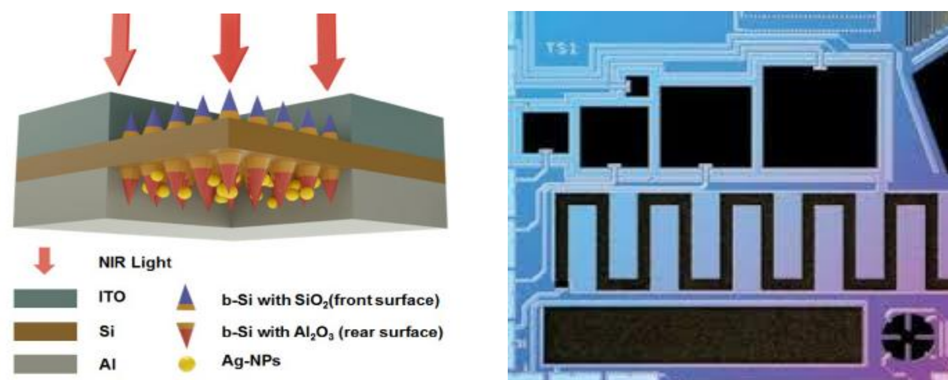

Figure 6 (a) Schematic diagram of near-infrared photodetector based on Schottky barrier and black silicon.[42] (b) Sulphur-doped black silicon-based photodetector.[6]

Photodetectors made of black silicon dramatically improve the sensitivity of silicon to visible radiation and significantly enhance broadband light absorption[42]. In particular, black silicon's NIR sensing properties potentially enable high-performance digital night vision capabilities comparable to the performance of existing image-intensifier-based night vision goggles. Figure 6(a) illustrates the schematic diagram of the near-infrared

photodetector based on the Schottky carrier [37]. Figure 6(b) shows the sulphur-doped black silicon-based photodetector, which is developed by the SiOnyx company [43]. The use of metal nanoparticles as plasmon absorbers and sulphur as a dopant for enhanced NIR sensitivity has been confirmed. Black silicon-based detectors already possess high sensitivity to optical waves with wavelength range from 400 to 1250 nm. However, the challenges for improving these materials are novel structural design and enhancing the response sensitivity to wavelengths over 1300 nm.

This thesis focuses on developing novel black silicon with hierarchical micro and nanostructured textures[44], [45]. The research goal of this thesis is to combine the advantages of multiscale surface structures and LSPR particles to enhance the anti-reflection properties of black silicon. In addition, potential applications involving photo-thermal-electric, photoelectric, and super-hydrophobic fluid control are also explored.

2 Black silicon fabricated via reactive ion etching

Black silicon with multiscale surface structures have been fabricated by various methods, including femtosecond laser pulse, reaction ion etching (RIE), electrochemical corrosion, and metal-assisted chemical etching.

The fabrication of new surfaces causing black silicon behaviour by laser irradiation is a frequently used method. According to different laser pulse durations, laser irradiation methods used for preparing black silicon are divided into femtosecond laser irradiation and nanosecond laser irradiation. Figure 7(a) displays the principle of femtosecond/nanosecond laser irradiation using a femtosecond laser to irradiate the silicon surface under corrosive gas SF_6. These high-energy lasers prompt the sulfur hexafluoride to react with the irradiated silicon to form the ablated nanocone surface texture. In this process, femtosecond laser treatment with chalcogenides should be performed to dope silicon with sulphur and oxygen to yield impurity energy levels[35], [46], [47]. These resulting impurity bands allow excited electrons to acquire indirect bandgap transition by absorbing two NIR photons, thereby providing intense trapping of NIR light. However, the control over the distribution of each level and number of impurities is quite challenging. Moreover, the doping process is susceptible to thermal annealing and intensity of laser impulses combined with the high cost and significantly long fabrication time.

The fabrication of black silicon by metal-assisted chemical etching has commonly been used in the mass production of wafer-level silicon-based devices. Noble metals, such as gold and silver are utilized as etching catalysts[22], [48]. In general, metal nanoparticles are formed on surfaces through various approaches after cleaning and deoxidizing the silicon surfaces. Figure 7(b) and 7(c) summarize the reaction principle. The silicon substrates are placed in an etching solution. Nano-conical or wire-like structures are then formed on material surfaces through the catalytic action of surface metal nanoparticles. Noble metal nanoparticles serve as transport media for reaction intermediates like electric charges and reaction products during the catalytic process. The main techniques used to deposit metal nanoparticles are based on thermal

evaporation, post-coating heat treatment, and chemical solution formation. These metal-assisted chemical etching methods are advantageous in terms of low cost. However, they still suffer from the difficulty of fabricating complex three-dimensional (3D) devices with highly-ordered and large-size structural configurations due to their high dependency on crystal orientation.

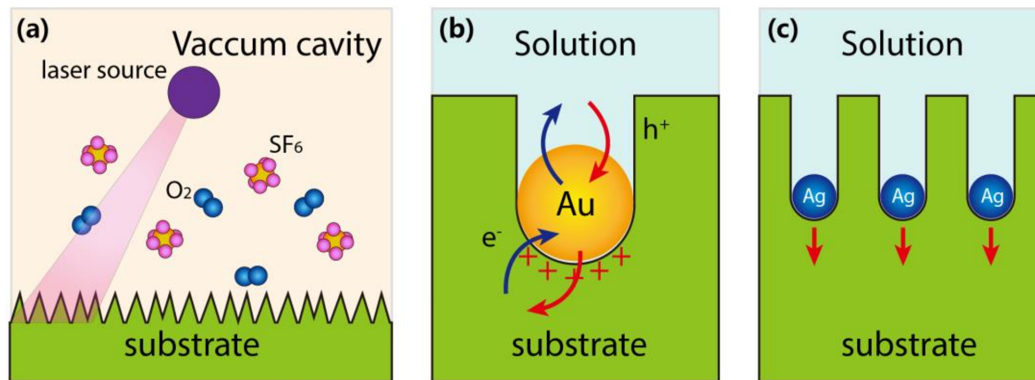

Figure 7 Schematic diagram of the laser irradiation process (a) and the metal-assisted chemical etching process using (b) gold and (c) silver.

Among the methods mentioned above, dry etching is advantageous for controlling the anisotropic etching and high precision nano-patterning.

Reactive ion etching is a dry etching technology with excellent anisotropy and high selectivity [32], [49]. This process uses molecular gas plasma to etch substrate materials in a vacuum system. The process employs molecular gas plasma to etch substrate materials in vacuum systems. Under these conditions, gas plasma yields ion-induced chemical reactions with the substrate, resulting in anisotropic etching. The ion energy of plasma is important for the formation of etched damage layers on surfaces of etched layers, as well as facilitating the occurrence of chemical reactions. Meanwhile, gas plasma ions could also remove surface products to expose clean etched surfaces. However, this etching technique is not suitable for obtaining high selection ratios. It also induces damage to substrate surfaces and causes pollution, making the formation of delicate patterns more difficult. By comparison, deep reactive ion etching (DRIE)[50] is a silicon etching technology that uses fluorine-based gas to achieve high aspect ratio

profiles. The principle of DRIE is similar to that of RIE, in which silicon anisotropy is employed to chemically and physically etch silicon surfaces. Two radio frequency sources are utilized to separate plasma generation from self-bias voltage generation, effectively preventing the contradiction between radio frequency power and plasma density during RIE etching. The Bosch process is representative of DRIE based on alternate etching and passivation steps[51]–[53]. This controllable lateral etching process could protect sidewalls with steep or other inclined angles.

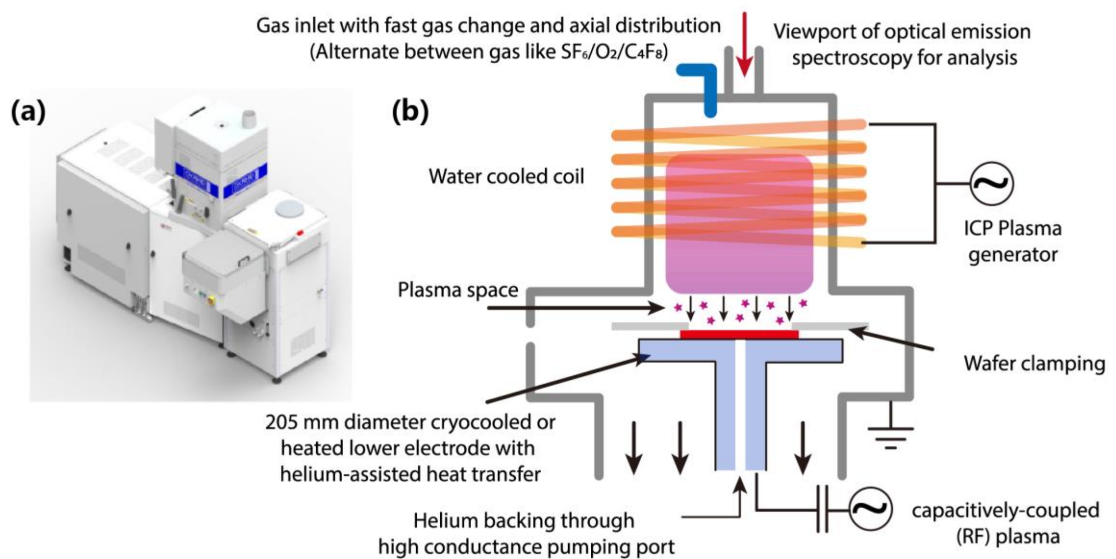

Figure 8 (a) Oxford Plasma Pro100 instrument. (b) Schematic diagram of basic Bosch etching principles.

2.1 Bosch etching process

Bosch etching, a widely used dry etching approach, originates from anisotropic silicon etching. It was developed by Robert Bosch in Germany and is also referred to as the Bosch gas-switching technique. Figure 8(a) shows an image of the Oxford Plasma Pro100 instrument used to generate the results in this thesis. The Plasma-Pro 100 etching and deposition tool can be applied to various substrate electrodes and can process over a wide range of temperatures. The 150 mm-size clamping platform allows the processing of a single wafer from 4-inch to 6-inch. The most striking thing is that the machine provides excellent homogeneity and high throughput, high precision process. As shown in Figure 8(b), the core vacuum etching module features separate ICP and capacitively-

coupled (RF) plasma sources, independent plasma density control, and ion energy. The ICP plasma generator has a frequency of 2.4 MHz and can be operated at powers up to 2500 W. In contrast, the RF generator produces up to 300 Watt plasma and has a frequency of 13.56 MHz. Both generators are impedance matched to the plasma with two tunable vacuum capacitors each. As a result, high ion densities (>1011cm^{-3}) and high radical densities can be achieved, and the generated ions depend on the gas mixture. In addition, the load-lock module and the auto-transfer arm permit rapid sample transfer without contamination of the vacuum etching chamber. For the Bosch etching process, the plasma source is applied to form the anisotropic etching reaction and polymeric passivation layer. These two processes alternately repeat to achieve anisotropic etching. A commonly used gas in silicon etching processes is SF_6 (sulphur hexafluoride). Sulphur hexafluoride generates 6 fluorine atoms under a voltage of only 20 eV. The produced fluorine atoms interact with Si to form volatile SiF_4 (silicon tetrafluoride). A lithographic mask pattern occupies about 15% of the 6-inch silicon wafer die area. The etching operating conditions are: plasma reaction chamber pressure >30 mtorr, SF_6 flow >400 sccm, and radio frequency (RF) energy up to the kilowatt level. Theoretically, the etching rate reaches 20 µm/min. To achieve a high-rate polymer deposition reaction, the ratio of F to C in the gas generated by the plasma reaction must be less than or equal to 2:1 (i.e., F:C ≤ 2:1). CHF_3 (trifluoromethane) and C_3F_8 (octafluoropropane) cannot meet this requirement, but C_4F_8 (octafluorocyclobutane) can be used. C_4F_8 is also commonly used as the additive gas in plasma etching oxidation reactions. This polymer deposition reaction leads to the adjustable formation of a sidewall passivation layer and improves the selection ratio of the mask materials (such as the photoresist and silicon dioxide). During Bosch etching, the C_4F_8 and SF_6 gases are mixed, and alternate stratification is the key to produce a crenelated and anisotropically etched sidewall. After the etching loops are complete, the deposited polymer masking film is easily removed by the addition of O_2 plasma.

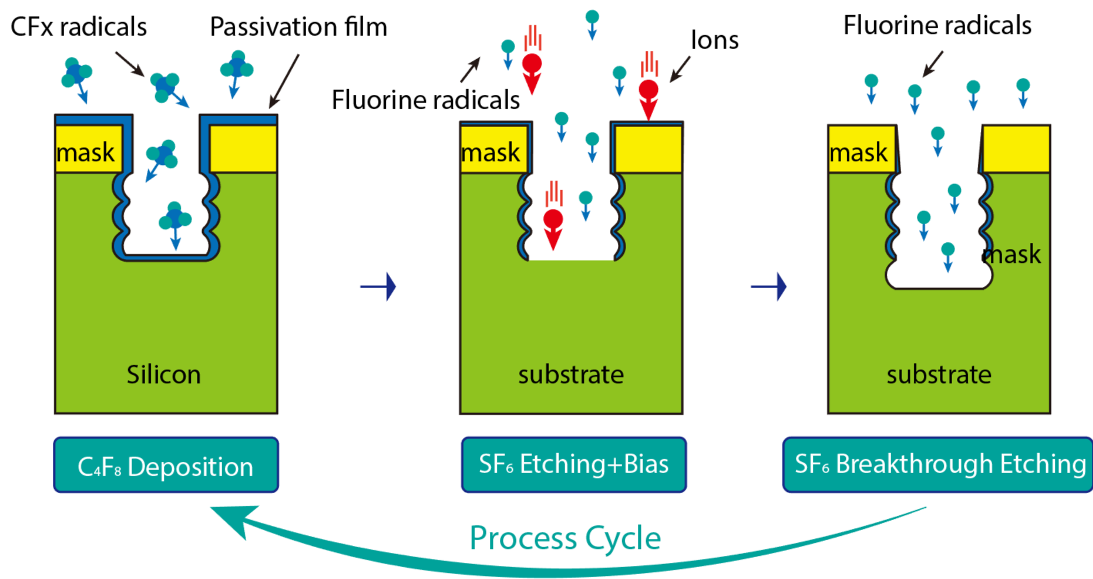

Figure 9 Schematic diagram of the Bosch etching process.

In the Bosch process, the plasma source is first enabled with SF_6 gas input to generate the F-rich plasma atmosphere. The exposed silicon substrate is briefly etched. Figure 9 shows that the first etching step is dominated by fluorine ions and leads to isotropic etching. The second step is a quick switch to the passivation operation with C_4F_8 gas. In this step, the plasma source is turned off to generate a polymer protection layer on both the silicon and the mask. These sequentially alternating etching and protection steps form a single etching loop, which is then repeated. The next loop first removes the polymer used for protection in the prior loop, and the polymer at the bottom of the etched surface is more significantly removed than that on the sidewall. Therefore, some polymer is still present on the sidewall when the bottom polymer is completely removed, and etching will consume the underlying silicon. The sidewall is protected while the bottom silicon is etched. When the silicon is etched to the same level as the first loop, the next passivation step stars. In this way, the bottom becomes deeper, the etching time is precisely controlled, and no undercutting occurs. The sidewall is protected and stays vertical during the alternating etching and passivation steps. While each cycle's achieved depth is not large, the continuous cycles result in a deep and very steep etching profile. Due to the high chemical reactivity of fluoride ions, the overall Bosch process

reaction proceeds very rapidly. In general, Bosch etching has a high rate and leads to high steepness and a high aspect ratio.

The first chemical reaction that occurs in the passivation step is as follows:

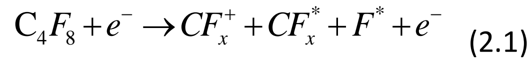

$$C_4F_8 + e^- \rightarrow CF_x^+ + CF_x^* + F^* + e^- \quad (2.1)$$

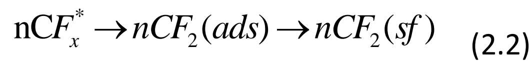

$$nCF_x^* \rightarrow nCF_2(ads) \rightarrow nCF_2(sf) \quad (2.2)$$

The passivation gas C_4F_8 dissociates and polymerizes again to form a polymer layer that protects the sidewall. As shown in Figure 10(a), an nCF_2 passivation layer is deposited on the silicon surface and the mask layer.

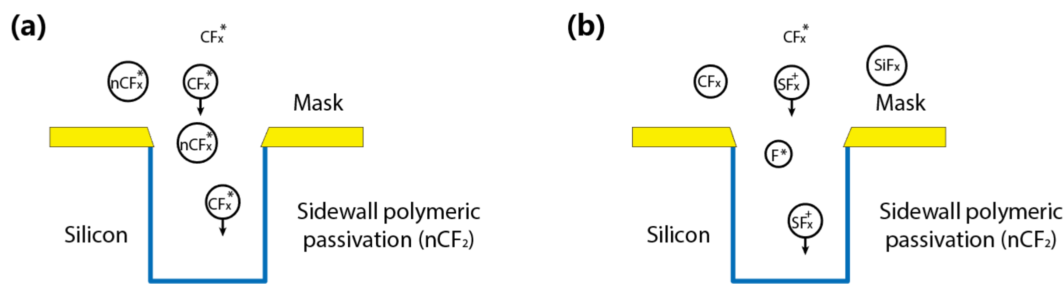

Figure 10 Etching and passivation steps in the Bosch process. (a) Passivation and (b) etching.

The chemical reactions in the etching step, as shown in Figure 10(b), are as follows:

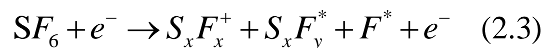

$$SF_6 + e^- \rightarrow S_xF_x^+ + S_xF_y^* + F^* + e^- \quad (2.3)$$

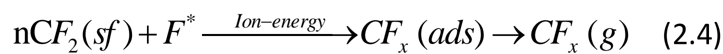

$$nCF_2(sf) + F^* \xrightarrow{Ion-energy} CF_x(ads) \rightarrow CF_x(g) \quad (2.4)$$

SF_6 is ionized under electron bombardment, and the generated active fluoride ions react with and remove the passivation layer on the surface. The fluoride ions then continue to react with silicon to etch the surface in areas where the passivation layer has been completely removed:

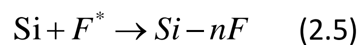

$$Si + F^* \rightarrow Si - nF \quad (2.5)$$

$$\text{Si} - nF \rightarrow SiF_x(ads) \quad (2.6)$$

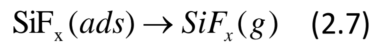

$$\text{SiF}_x(ads) \rightarrow SiF_x(g) \quad (2.7)$$

The real physical and chemical processes carried out in the plasma environment are complicated, and it is difficult to conduct whole-scale observations and accurate measurements. The chemical reactions described in this section are those widely recognized by researchers. There is not yet a unified and detailed theoretical explanation for the Bosch process.

Figure 11 shows the relationship between the main parameters of the Bosch etching process. The arrows show the influence of the process parameters in relation to each other[54], [55]. The etching rate increases with the plasma power and SF6 etching time; in the meantime, the required number of process loops decreases. On the other hand, the rapid increment of plasma power and etching time is easy to cause isotropic etching due to the overconsumed passivation layer.

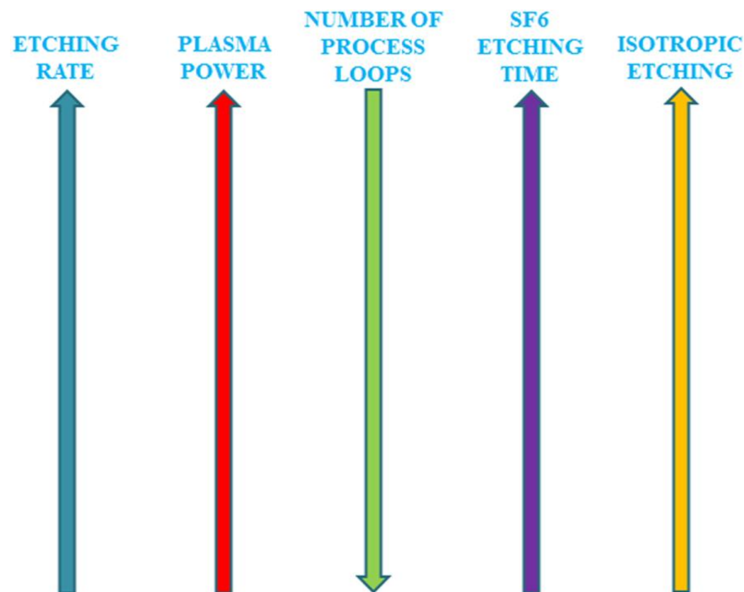

Figure 11 Relationship between the main parameters of the Bosch process.[56]

2.2 Reactive ion etching using SF_6 and O_2 mixture

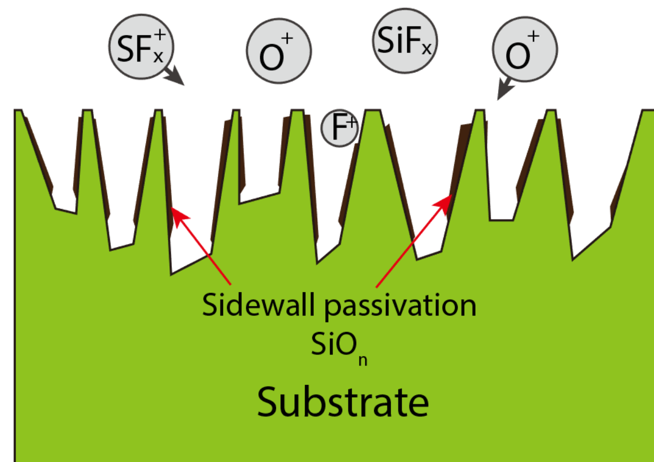

Figure 12 Schematic diagram of reactive ion etching with a mixture of SF_6 and O_2.

As is well-known, selectivity, etching rate, and anisotropy are crucial in dry etching processes[57]. Anisotropy is controlled by changing the etching chemistry mechanism, which is usually achieved by introducing other gases to modify the gas-solid interaction. For instance, adding oxygen to SF_6 plasma can create a chemically inert layer at etched sites[58]. This inert layer, composed of neutral oxyfluorides, acts as an etching inhibitor and passivates the silicon surface, as depicted in Figure 12. The passivated surfaces lead to a decrease in the lateral etch rate and an increase in the etch profile's anisotropy. This process has been applied for manufacturing nanoscale structures.

SF_6 plasma is composed of F^+, SF^+, SF^{3+}, and SF^{5+}. With the addition of O_2, the plasma also contains O* radicals. The SF^{x+} ($x \leq 5$) and F^+ ions are bombarded into the silicon substrate by the bias voltage. These reactive ions interact with silicon to form volatile SiF_4, which escapes from the substrate, while O* radicals react with the silicon to rapidly form SiO_x. The SiO_x reacts with SF^{x+} ($x \leq 5$) and F^+ ions to form neutral oxyfluorides ($Si_xO_yF_z$) such as SOF_2, SO_2F_2, and SOF_4 because the binding energy of Si–F bonds (129.3 kcal/mol) is higher than that of Si–O bonds (88.2 kcal/mol). These oxyfluorides form a polymer-like layer on the etched surface and present a nonuniform thickness. Some of the oxyfluorides escape from the substrate, and the exposed silicon surface reacts with SF^{x+} ($x \leq 5$) and F^+ ions. The remaining polymer layer acts as a randomly perforated mask

and accumulates to passivate the surface during the follow-up etching. Both the reactive ion-induced etching and oxyfluoride accumulation-induced passivation simultaneously take place. As a result, the etching reaction is blocked in areas with thicker passivation layers. In contrast, rapid etching takes place in the exposed regions covered with less or no polymer. This leads to a selective and depth-directed etching of the exposed silicon, resulting in hole or needle-like structures. The formed structures vary under the competition of the SF^{x+} ($x \leq 5$) and F^+ ion etching effect, polymer-like passivation, and ion bombardment, meaning that the SF_6/O_2 gas ratio determines the structure profile. When the SF_6/O_2 gas ratio is low, polymer passivation plays a governing role and hole-like structures are formed. With an increasing SF_6/O_2 gas flow ratio, the SF^{x+} ($x \leq 5$) and F^+ ion etching effect dominates and a needle-like structure is formed.

In this thesis, a novel SF_6 and O_2 gas flow ratio of 36 to 47 is used. This ratio is an original creation and was developed at the University of South-Eastern Norway. The detailed process is introduced in Section 3.1. Top view and side view scanning electron microscope (SEM, Hitachi UHR FE-SEM SU8230, Japan) images of the achieved needle-like structure are shown in Figure 13(a) and (b). From the top view, the surface structures appear as continuous holes, while they are needle-like structures with different heights at the tilted view.

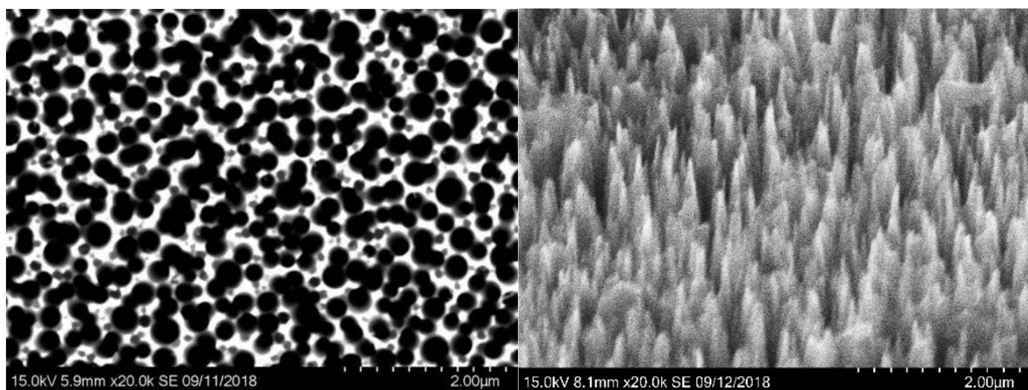

Figure 13 (a) Top view and (b) side view SEM images of the achieved needle-like structure obtained via reactive ion etching with a mixture of SF_6 and O_2.

2.3 Inspiration

Black silicon materials previously reported by other researchers mainly have various nanostructures such as nanopores, nanocones, and nanorods. These structures have high aspect ratios and densities that change and extend the propagation path of incident light and attenuate the light through diffuse reflection, refraction, and direct absorption, resulting in a unique light-trapping ability. This allows black silicon to have a high light absorption performance. Black silicon has been widely studied in photoelectric, photothermal, photochemical, and light-controlled microfluidic applications. However, in existing applications, nanostructured black silicon still has disadvantages. For example, as illustrated in Figure 14(a), thin films fabricated by physical or chemical vapour deposition cover the original structure pitch, resulting in reduced aspect ratios and weakened light-trapping capability. Figure 14(b) shows a photocarrier reacting with ions and producing gas bubbles that accumulate at the solid-liquid interface. The gas bubbles adhere to the black silicon's hydrophobic nanostructured surface and act as an isolation layer to hinder the reaction. Figure 14(c) shows a light-controlled microfluidic black silicon material for cell screening. The size of the target cells differs from that of other body cells. Therefore, the fixation and screening of these cells are difficult to achieve on black silicon surfaces with single-sized structures. Furthermore, nanostructured surfaces are vulnerable during operation, as depicted in Figure 14(d), and it is not easy to remove pollutants.

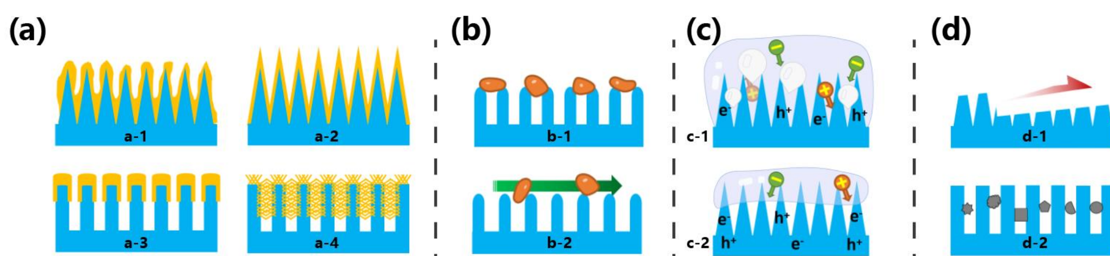

Figure 14 The disadvantages of black silicon materials containing only nanostructures. (a) The nanostructure pitch with size below tens to hundreds of nanometers is buried by the deposition of functional materials via (a-1) chemical deposition, (a-2) atom layer deposition, (a-3) sputtering, and (a-4) epitaxial growth. (b) Cell screening by a microfluidic black silicon surface, where (b-1) target cells are

unable to be fixed and (b-2) the target cells are easily removed by fluid flow due to the intrinsic small pitch size. (c) The slow desorption of product gas bubbles and the poor wetting contact of the solid interface and reaction liquid, which reduces the reaction speed, as depicted in (c-1) and (c-2). (d) The nanostructured surface is vulnerable to (d-1) friction and (d-2) surface residues, which are difficult to remove.

Emerging microfabrication technologies allow the production of black silicon with variable size surface textures from the nanoscale to the microscale. **Therefore, why not introduce micron-sized structures and combine the advantages of micro and nanostructures on black silicon?** This micro-nano composite design is expected to enhance the specific surface area and space and form a large structure size difference in three-dimensional space. The introduction of micron structures would be advantageous in many aspects, as illustrated in Figure 15. Enlarged specific surface areas for depositing engineering materials and avoiding a decline in aspect ratios caused by a buried pitch is achieved, as depicted in Figure 15(a). Meanwhile, the micro-holes could serve as protection zones for preventing target cells from flowing away with the solution (Figure 15(b)). Also, the micro-holes may expand the contact between the solid-liquid interface, as well as modify the hydrophilicity and hydrophobicity of the surface (Figure 15(c)). The hierarchical configuration of micro and nanostructures may also prevent surface damage, as shown in Figure 15(d).

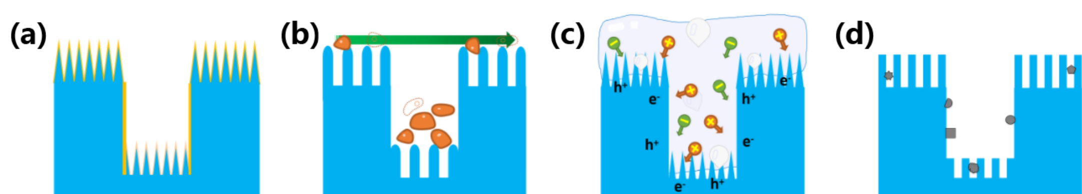

Figure 15 The advantages caused by the introduction of microstructures. (a) Enlarged specific surface area. (b) Creation of protection zone for target cells. (c) Expanded solid-liquid contact area. (d). Hierarchical configuration of micro and nanostructures preventing surface damage.

The most attractive property of black silicon has to do with its light-trapping effect. Therefore, surface texturing black silicon could strengthen its light-trapping ability as

much as possible. The light-trapping capability originates from the change in optical propagation caused by multiple reflections, as well as energy decay caused by light-silicon coupling. Recently, light-trapping through hybrid structures has attracted increasing research attention. The hybridization of micro-nano scale structures could increase the light-trapping ability of black silicon. Compared to conventional nanostructures, microscale structures have larger feature sizes and quickly form ordered arrays with straight pores and adequate space. Besides, the introduction of microscale textures offers large dimensional variations, enabling the design and fabrication of complex 3D spaces.

In this thesis, more attention is paid to the hybridization of needle-like nanostructures formed by SF_6/O_2 reactive ion etching, as well as microstructures with vertical and smooth sidewalls created by Bosch etching. The perpendicular smooth sidewalls would benefit the propagation of direct incident light along the depth direction. The microstructures would also provide large windows for incoming light. These microstructures showed comparable dimensions to larger wavelengths, meaning that multiple reflections would take place inside the structures. However, incident light may escape from these microstructures via mirror reflections. The needle-like nanostructures are used as excellent candidates to avoid reflection losses. Therefore, incident light could undergo sudden refractivity changes and diffuse reflections due to needle-like structures' smaller dimensions compared to incident light wavelength. In this thesis, needle-like nanostructures are used to decorate the smooth top surface areas of microstructured holes with smooth vertical sidewalls to decrease direct mirror reflection loss. Nanostructures at the bottom of the microstructures may also affect the reflection behaviour of light, thereby enhancing the light-material coupling effect. As a result, the reflection changes and light-material coupling effect caused by the hybridization of perpendicular micro and nanostructures could significantly raise the incident light energy decay.

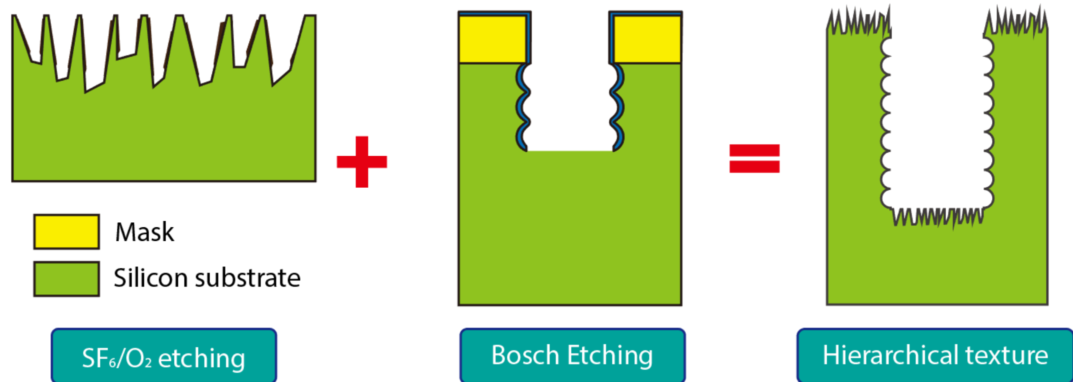

Figure 16 Schematic diagram showing the principle of the two-step etching process to produce a hierarchical texture on a black silicon surface.

Therefore, this assumption inspires us to explore the anti-reflective properties of a hierarchical design that integrates vertical micron-sized structures with nanometric decorations on their top surface and bottom area. As depicted in Figure 16, a two-step etching process involving SF_6/O_2 RIE and Bosch etching steps is developed to produce novel black silicon. The Bosch etch step aims to form micropores with vertical sidewalls and the RIE treatment with SF_6/O_2 is to form high-aspect ratio nanopores on the smooth top and bottom of the micropores. The resultant black silicon has hierarchical surface textures combining micro and nanostructures. This method may significantly address the disadvantages of black silicon surfaces made of only nanostructures.

3 Novel black silicon fabricated via two-step reactive ion etching

3.1 Honeycomb-like black silicon

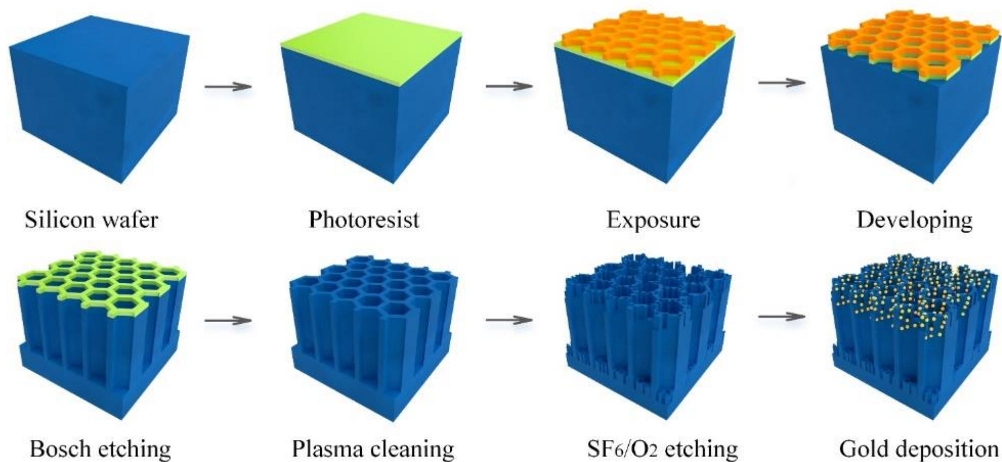

Figure 17 Honeycomb-like black silicon fabrication schematic diagram. The fabrication consists of two major steps: Bosch etching with a mask to form an ordered micro honeycomb array and RIE with a mixture of SF_6 and O_2 to form disordered nanopores.

First, honeycomb-like black silicon is created through two etching steps, as shown in Figure 17. The first step is Bosch etching with a mask to form ordered micropores, which are arranged in a honeycomb pattern. The second step is maskless reactive ion etching with SF_6/O_2 to form disordered nanopores. Gold nanoparticle deposition is conducted to form a localized surface plasmon resonance (LSPR) effect to increase near-infrared light absorption[33], [59], [60]. This material is further detailed in Chapter 4.

This honeycomb-like black silicon is developed on a p-type <100> wafer (resistivity of about 10-30 Ω cm). The positive photoresist S1813 is employed to achieve the high-resolution mask pattern for Bosch etching. The pitch and diameter of the honeycomb-like pores vary from 2 to 10 µm, while the depths are 10 to 75 µm. The pore depth is highly controllable by setting the etching duration. The second etching with SF_6 (gas flow of 36 sccm) and O_2 (gas flow of 47 sccm) provides a rapid bombardment of the fresh silicon surface and generates a passivation layer of SiO_x, which acts as a mask to block

continuous etching breakthrough. This results in a randomly distributed nanopore surface without the help of a photoresist mask. As a result, the nanopores decorate both the top and bottom of the honeycomb-like micropores.

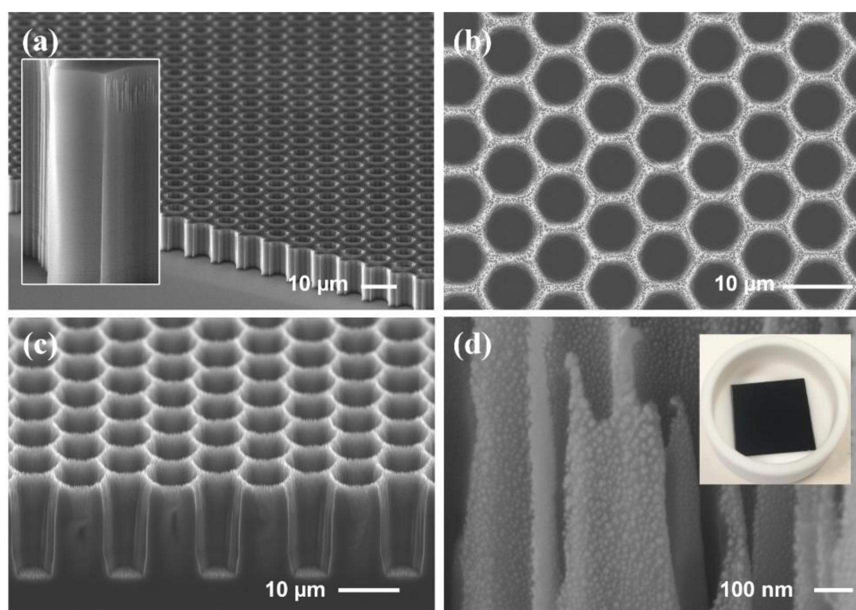

Figure 18 SEM micrographs of the honeycomb-like black silicon. (a) Tilted view of the honeycomb pores. The inset shows an enlarged view of a sidewall. (b) Top view of the surface decorated with nanopores. (c) Tilted view of the honeycomb pores decorated with nanopores. (d) Distribution of gold nanoparticles on top of the nanopores. The inset is a digital photograph of the black silicon after gold nanoparticle deposition.

Details of the fabrication process are reported in Table 1 and Table 2. The use of a high bias potential and a low table temperature realize high-speed directional etching and vertical honeycomb pore sidewalls, as shown in Figure 18(a). The unique SF_6 and O_2 gas ratio realizes nanopores with a high aspect ratio. As a result, the top surface and the bottom of the honeycomb pores are both decorated with nanopores, as shown in Figure 18(b) and (c). Figure 18(d) shows the gold nanoparticles deposited on top of the nanopores. The gold nanoparticles induce an LSPR effect to increase the absorption of near-infrared light, which is explained in further detail below.

Table 1. Mask-assisted Bosch etching process details.

Main steps in each etching loop	SF_6 gas flow (sccm)	C_4F_8 gas flow (sccm)	ICP power (W)	HF power (W)	O_2 gas flow (sccm)	Table temperature (˚C)	Pressure (mTorr)	Helium backing (Torr)	Step time (ms)
Pre-Deposition	10	200	1500	5	0	5	20	10	25
Deposition	5	120	1250	5	0	5	20	10	550
Deposition Sub 1	20	120	1250	5	0	5	20	10	50
Deposition Sub 2	160	120	1250	5	0	5	30	10	100
Deposition Sub 3	160	5	2000	5	0	5	30	10	50
Deposition Sub 4	160	5	2000	60	0	5	30	10	50
Breakthrough	160	5	2000	60	0	5	30	10	325
Breakthrough sub1	160	5	2000	60	0	5	30	10	100
Breakthrough Sub2	160	5	2000	60	0	5	80	10	50
Breakthrough Sub3	160	5	2500	0	0	5	80	10	50
Etch	360	5	2500	0	0	5	80	10	200
Etch Sub1	1	120	2500	0	0	5	80	10	150
Etch Sub2	5	120	1250	0	0	5	20	10	100

Table 2. Maskless reactive ion etching with SF_6/O_2 process details.

Process parameter	ICP power (W)	HF power (W)	SF_6 gas flow (sccm)	O_2 gas flow (sccm)	C_4F_8 gas flow (sccm)	Table temperature (˚C)	Pressure (mTorr)	Helium backing (Torr)	Cycle time (s)
Value	1500	50	36	47	0	0	35	10	300–1200

3.2 Chimney-like black silicon

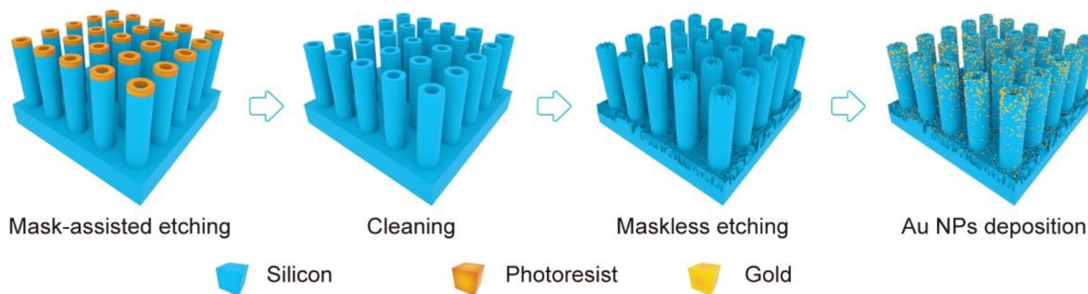

Figure 19 Schematic diagram of chimney-like black silicon fabrication process.

Based on the honeycomb-like black silicon fabrication process, the two-step etching process is also employed to develop a chimney-like black silicon material. As illustrated in Figure 19, the fabrication process consists of four significant steps: (1) mask-assisted etching (Bosch RIE) to construct hollow cylinders, (2) cleaning the residual photoresist, (3) maskless RIE (with SF_6/O_2) to decorate the top and bottom surfaces with nanopores, and (4) deposition of Au nanoparticles via magnetron sputtering and thermal annealing. Optimizing the Au NP configuration is the key to achieving ultralow reflection in the broad wavelength range of 220 to 2600 nm, which is discussed in Chapter 4. Figure 20 (a) and (b) show side and top views of the black silicon with nanopores obtained via RIE with SF_6/O_2, skipping the mask-assisted Bosch etching step. Figure 20 (c) and (d) show a tilted view of a hollow cylinder array and a tilted view of the chimney-like black silicon combining the hollow cylinders and nanopores. The inset image shows a magnified chimney decorated with the nanopores. Figure 20 (e) and (f) show digital photographs of 4-inch textured silicon with a hollow cylinder array, with only nanopores, and the chimney-like black silicon containing both a hollow cylinder array and nanopores.

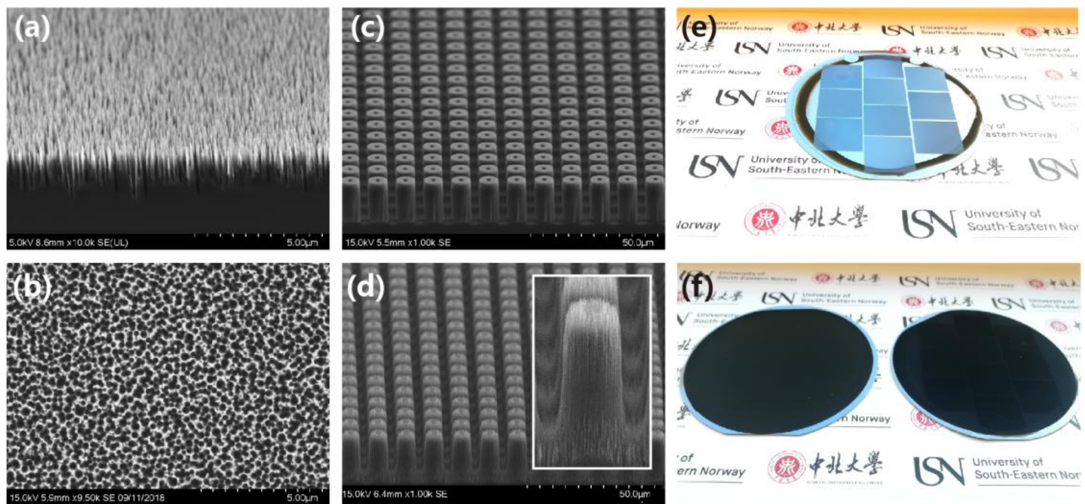

Figure 20 (a) Side view and (b) top view of black silicon with nanopores obtained via RIE with SF_6/O_2, skipping the mask-assisted etching step. (c) Tilted view of textured silicon hollow cylinder array. (d) Tilted view of chimney-like black silicon with hollow cylinders and nanopores. The inset image shows a magnified chimney decorated with nanopores. (e) Digital photograph of textured silicon with a cylinder array. (f) Digital photographs of 4-inch nanopore black silicon wafer (left) and chimney-like black silicon wafer with both a cylinder array and nanopores (right).

Optimizing surfaces by modifying the diameter, spacing, and height of surface structures is also crucial for studying the anti-reflectivity of chimney-like black silicon. Figure 21(a), (b), and (c) show three different silicon arrays with different hollow cylinder diameters, spacing, and height variations. The SEM images in Figure 21 (a) and (b) illustrate the cylinder diameter set of 10, 8 µm and the pitch set of 2, 4 µm, respectively. The resultant heights are both 20 µm. Figure21 (c) shows the cylinder diameter of 8 µm and the pitch of 2 µm. The resulting cylinder has a height of 31 µm. The reflectance of the samples above will be investigated in chapter 4.2.

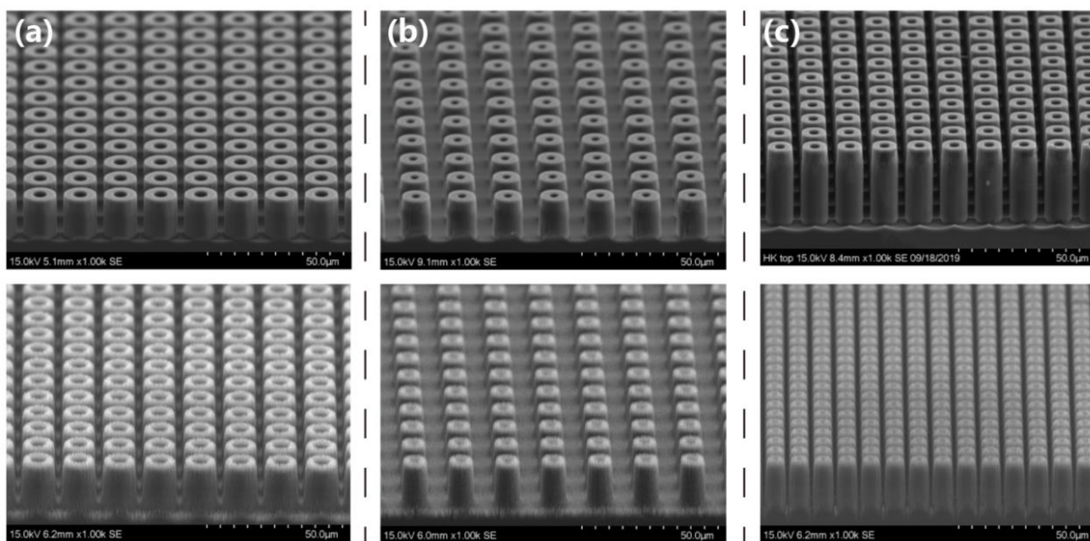

Figure 21 SEM images showing tilted views of silicon surfaces with only hollow cylinder arrays (upper images) and chimney-like black silicon surfaces with both hollow cylinders and nanopores (lower images). (a) SEM images of samples with cylinder diameters of 10 µm and a pitch of 2 µm. (b) SEM images of samples with cylinder diameters of 8 µm and a pitch of 4 µm. (c) SEM images of samples with cylinder diameters of 8 µm a pitch of 2 µm, and heights of 31 µm.

3.3 Nanowire black silicon

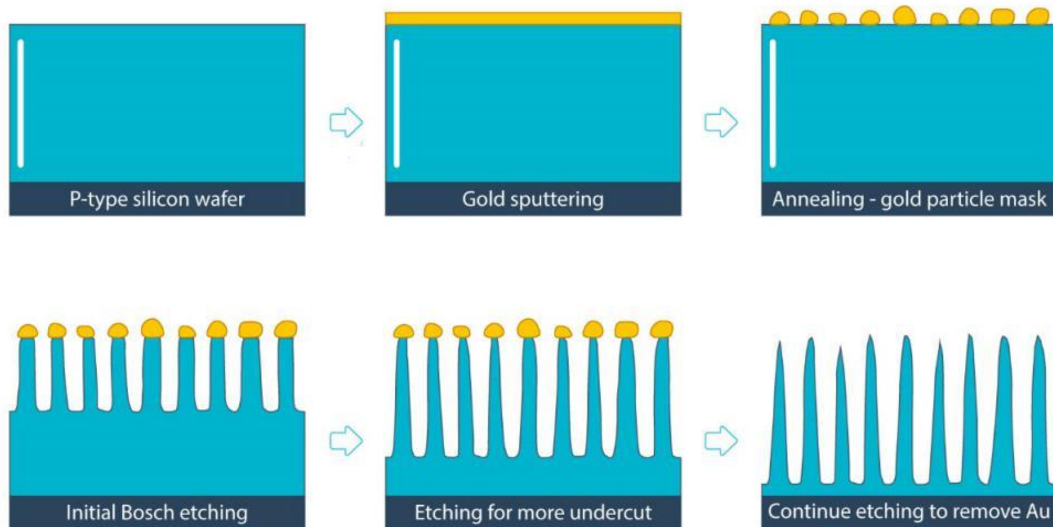

Figure 22 The scheme for the fabrication of the Nanowire black silicon. The fabrication process consists of gold sputtering and annealing to form a gold particle mask, followed by three etching steps: an initial Bosch etching, undercut etching, and further etching to remove the gold nanoparticles.

Figure 22 shows a two-step process for fabricating nanowire black silicon. This process consists of gold sputtering and annealing to form a gold particle mask. The followed treatment includes three etching steps of the initial Bosch etching, undercut etching, and further etching to remove the gold nanoparticles. The first line of diagrams involves sputtering a gold film and then annealing it at 500 °C for 1 h to generate a particle mask. The second line illustrates a three-step modified Bosch etching process.

Table 3. Details of the modified Bosch etching process for fabricating nanowire black silicon.

Process parameter	Value
ICP power	2500/1250 W
HF power	100/5/60/0 W
Pressure	20 mTorr in strike step; 30 mTorr in deposition step; 30 mTorr in breakthrough step; 80 mTorr in etching step
Main deposition step	C_4F_8 – 60 sccm; SF_6 – 5 sccm
Main breakthrough step	SF_6 – 500 sccm; C_4F_8 – 5 sccm
Main etching step	SF_6 – 500 sccm; C_4F_8 – 5 sccm
Table temperature	0 °C
Total cycle	80–160 loops

The etching experiments are carried out in a helicon antenna-coupled plasma reactor. A turbo-vacuum pump is applied to adjust parameters such as gas flow and plasma reactor pressure, resulting in the quick change and precise control of the plasma density. The single etching loop is composed primarily of three steps: the deposition of the protective layer, the breakthrough of the bottom layer, and the etching of the depth direction. As detailed in Table 3, in the first step, repeated C_4F_8 flows of up to 60 sccm (standard cubic centimeters per minute) are used to deposit a protective layer on both the metal nanoparticles and the pore sidewalls, resulting in a thick polymer coating on both the metal nanoparticles and pore sidewalls. This thick polymer wrapping of the metal nanoparticles is beneficial for avoiding mask undercut, achieving a high selection ratio between the particle mask and silicon. The following deposition step uses a C_4F_8 flow rate of 5 sccm to form a thin protection polymer layer on the bottom of the pores. At the same time, etching is conducted by an SF_6 flow of up to 160 sccm to avoid excessive fast C_4F_8 deposition that would block the nanoscale structure interval spaces. The deposition and etching balance is adjustable according to the structure pitch size. Next, the bottom breakthrough step removes the protective polymer layer and exposes the silicon substrate at the pore bottom. Finally, the depth direction etching step produces highly anisotropic etching by reacting SF_6 with the bottom silicon quicker than the sidewall. The carrier for the etching pieces is a silicon wafer with an Au layer placed on its top surface. The temperature of the cooling carrier under the silicon wafer is set to 5 °C. To accurately control the temperature distribution of the etching pieces to be highly consistent with the setting value of the cooling carrier temperature, high thermal conductivity silicone grease is employed to bond etching pieces to the table silicon wafer. Gold nanoparticles are deposited to boost near-infrared light absorption to form a localized surface plasmon resonance effect, detailed in Chapter 4.

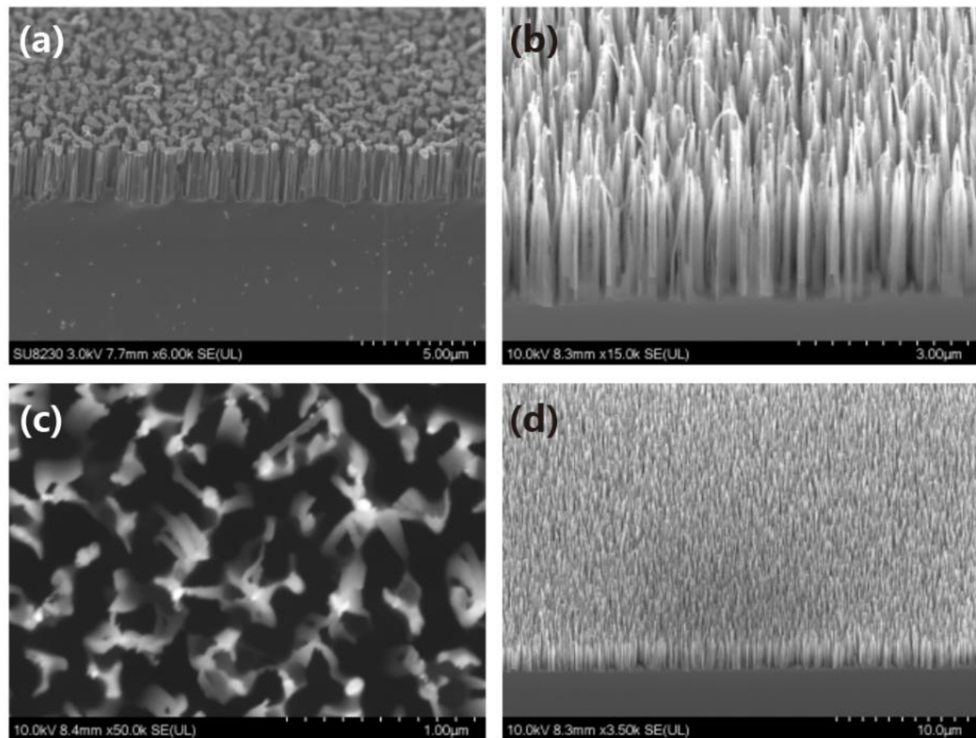

Figure 23 SEM images of nanowire black silicon fabricated via modified Bosch process. (a) Tilted view of the nanoparticle mask on the top of the nanowires. (b) Tilted view of the silicon nanowires. (c) Top view of the silicon nanowires. (d) Tilted view of the silicon nanowires at a lower magnification.

SEM pictures of silicon nanowires produced by 120 Bosch etching loops are shown in Figure 23. The etching mask is made out of nanoparticles produced by annealing a 4 nm Au thin film. Figure 23(a) displays Au nanoparticles with an average size of about 500 nm uniformly disperses on the top of the nanowires. Figure 23(b) shows a tilted SEM image of the nanowire array. The fabricated nanowires are vividly needle-like and have an average aspect ratio of about 10:1. It indicates that the depth direction etching step has a high selection ratio between the silicon and the mask and is highly anisotropic. It also demonstrates that the etch parameter set can prevent mask undercut and create structures with superior aspect ratios. Figure 23(c) shows a top view of the silicon nanowires, which exhibits a high proportion of pores that allows more incoming light and a low smooth surface proportion to avoid incident light reflecting away from the silicon surface structure. Figure 23(d) shows a tilted view of the silicon nanowires at a lower magnification, indicating that the nanowires are uniformly distributed. Photographs of the nanowire black silicon in pieces and as a wafer are shown in Figure

24. The nanowire black silicon in pieces (left) and wafer level (right) are all formed by using a 4 nm gold nanoparticle mask and 120-loops etching treatment. It is vividly indicated that the modified Bosch process and the applied Au-deposited carrier wafer is robust to produce nanowire black silicon.

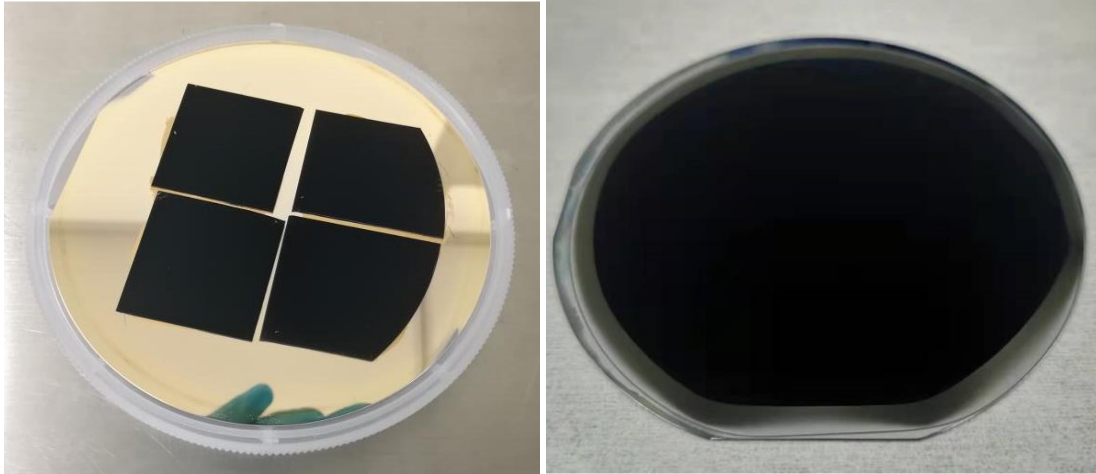

Figure 24 Photographs of the nanowire black silicon in pieces (left) and wafer level (right) formed by using a 4 nm gold nanoparticle mask and 120 etching loops.

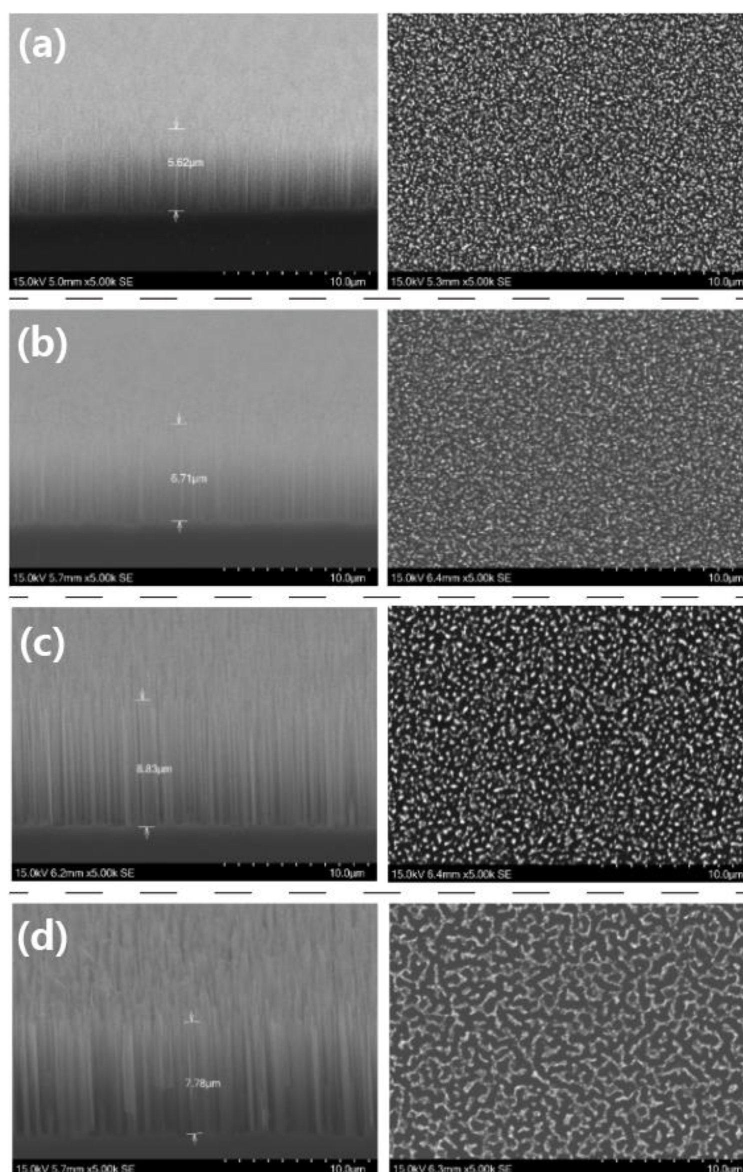

Figure 25 Tilted and top view SEM images of nanowire black silicon obtained by using (a) gold nanoparticle mask formed by 4 nm gold film and 160 etching loops, (b) gold nanoparticle mask formed by 6 nm gold film and 160 etching loops, (c) gold nanoparticle mask formed by 8 nm gold film and 160 etching loops, and (d) gold nanoparticle mask formed by 10 nm gold film and 160 etching loops.

One etching loop change and three different particle sizes are chosen to investigate the silicon nanowire formation caused by mask size and etching duration. Figure 25 shows photographs and SEM images of the silicon nanowires formed by a longer etching duration (160 vs. 120 etching loops) and varying the Au nanoparticle size. Figure 25(a) shows tilted and top views of silicon nanowires formed through 160 etching loops and

a 4 nm Au film to create the particle mask. The average height of the fabricated nanowires is 5.62 µm, suggesting that longer etching times result in taller nanowires. Figures 25(b), (c), and (d) show tilted and top views of the silicon nanowires etched by using particle masks formed with 6, 8, and 10 nm Au films, respectively. Their average nanowire heights are 6.71, 8.83, and 7.78 um, respectively. As particle size increases, the structural density decreases—silicon nanowires formed by the 4 nm Au film have the highest structure density. Because thicker films have a higher chance of accumulating and forming larger particles, particle intervals also become larger. Figure 24 shows a digital photograph of the nanowire samples obtained using particle masks formed by 4, 6, 8, and 10 nm Au films.

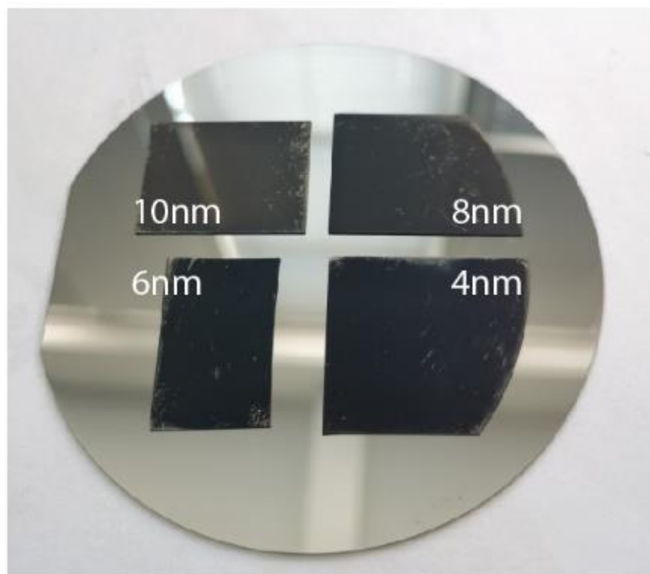

Figure 26 Digital photographs of the nanowire black silicon formed through 160 etching loops. The nanoparticle masks are formed by 4, 6, 8, and 10 nm Au films, respectively.

Figure 26 shows a digital photograph of the four nanowire black silicon samples fabricated using nanoparticle masks formed by 4, 6, 8, and 10 nm gold films, respectively. The etching duration for all four materials was 160 loops. The digital photograph comparison clearly shows that the nanowire surface induced by the presence of a 4 nm Au layer has the darkest appearance. Thus, this silicon nanowire sample is selected for further tests of optical characteristics and hydrophobicity measurements.

4 Light trapping and application of novel black silicon

4.1 Light trapping definition

The light-trapping ability of black silicon originates from the energy decay due to surface light reflections and the optical path length extension caused by internal refraction and transmission[8], [9], [61], [62]. The optical path length of optimal black silicon is generally several times the substrate bulk thickness, resulting in a light-trapping effect. The optical path length is the distance traveled by an unabsorbed photon within the silicon bulk before escaping from the substrate. The travel distance is generally expressed in terms of bulk thickness multiples. For example, the polished silicon substrate lacks a light-trapping feature, its optical path length equals one bulk thickness. In contrast, black silicon with good light trapping performance may have an optical path length of 50, indicating that light bounces back and forth many times within the silicon bulk.

The light-trapping effect is usually achieved by changing the incident angle that light travels into the silicon substrate. Black silicon' surface texture reduces reflections by refracting light obliquely into the silicon substrate, resulting in an optical path length longer than the substrate thickness. Snell's Law describes the angle at which light is refracted into the semiconductor substrate:

$$n_1 \sin\theta_1 = n_2 \sin\theta_2 \qquad (4.1)$$

where θ_1 and θ_2 are the light incident angles on the interface relative to the normal plane of the interface within mediums with refractive indices n_1 and n_2, respectively. θ_1 and θ_2 are shown in Figure 27 below.:

Angle θ_1 is smaller than angle θ_2 in a textured single-crystal silicon substrate due to the existence of crystallographic planes. Thus, the incident light comes into reflection and transmission on a textured silicon substrate.

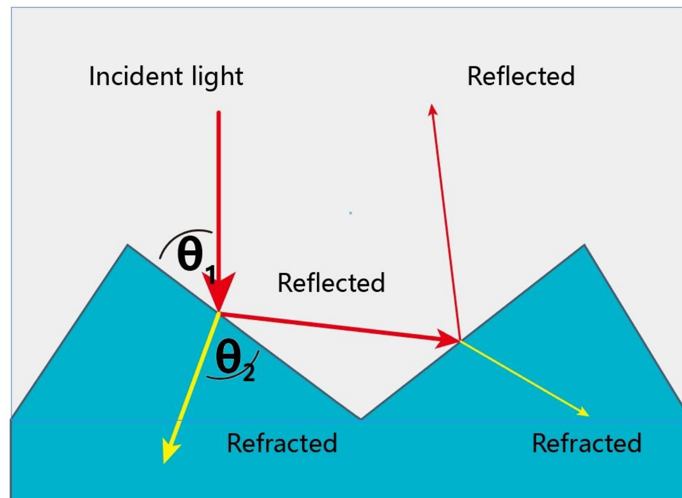

Figure 27 Reflection and transmission of light on a textured silicon substrate.

4.2 Light trapping on hierarchical surface texture

The light trapping mechanism on flat and textured silicon surface is explained in Figure 28. Incident light generates mirror reflections on flat silicon substrate into the surrounding environment, resulting in reflection loss shown in Figure 28(a). The reflected light reach the silicon surface at the same angle as the incoming light rather than being lost on a textured surface with smooth vertical micropores, reducing reflection loss and boosting coupling decay with the material, as shown in Figure 28. (c). Figure 28(b) shows a silicon surface with nanopores. The transmission of light within the material extends the optical path length and affects the reflection behaviour of nanopores with the same dimensional magnitude as the optical wavelength. The light waves propagating through the small nanopores exhibit refractivity change along with the depth direction, generating a moth-eye effect and a subsequent reduction in reflection. Figure 28(d) shows that micropores' smooth sidewalls also prolong the light path length by allowing multiple reflections and more light transmission. The combination of micropores and nanopores results in the ability to trap more light. The hierarchical surface texture formed by micro and nanopores facilitates the light-coupling effect with the silicon and increases the optical path length due to the micro-nano composite features.

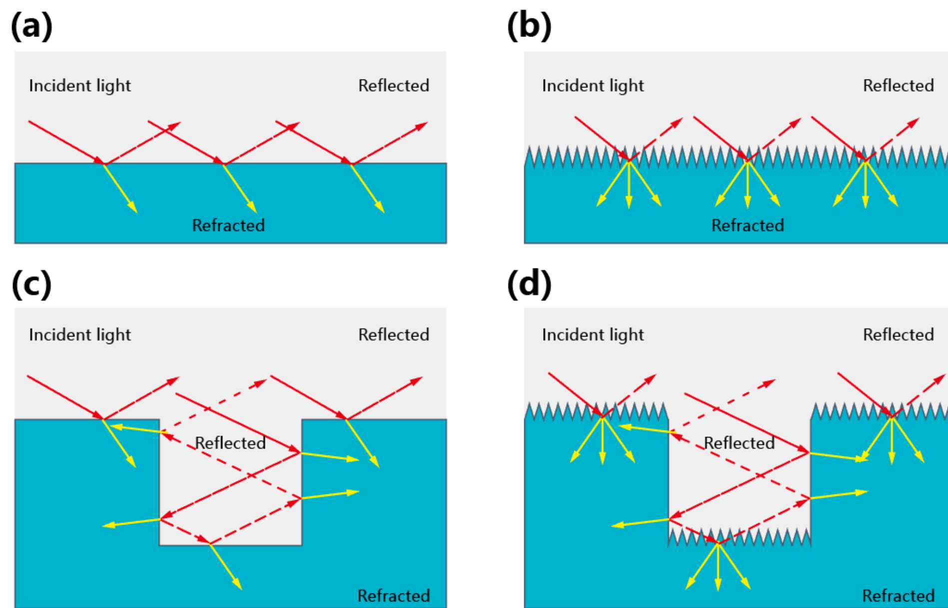

Figure 28 Schematic diagram of the anti-reflective principle of optical waves propagating through surfaces with different structural features: (a) flat surface, (b) surface with nanopores, (c) surface with micropores, and (d) surface with micro-nanopores.

Honeycomb-like black silicon samples with micropores of various diameters are fabricated to study the role of micropores systematically. The pore spacing of samples Si-1, Si-2, Si-3, and Si-4 is 2 µm, and the pore diameters of 2, 4, 6, and 8 µm, respectively. These samples have pore diameter to pore spacing ratios of 1 to 4. The reflectance of the surface-textured samples decrease in the whole wavelength range compared to planar silicon, as illustrated in Figure 29(a). The smooth surface area falls as the aperture to pore spacing ratio increases, leaving less surface area accessible for mirror reflections. Figures 29(a) and (b) show the sample Si-4 has the lowest value in transmittance. Therefore, sample Si-4 is selected to perform a second etching treatment. Figures 29(c) and (d) show the reflectance and transmittance difference between silicon samples with micropores, nanopores, micro-nanopores, and gold clusters samples. In the ultraviolet and visible wavelength range, black silicon with nanopores has nearly the same reflectance as samples with both micro and nanopores. However, the latter has lower reflectance and transmittance in the near-infrared range. The reflectance of black silicon with micro-nanopores sharply increases from 0% to about 30% when the light intensity is below the bandgap energy. It means that the light is no longer absorbed and can

scatter back out of the sample. But the transmittance of black silicon with micro-nanopores is very weak. In contrast to the silicon specimen with only micro or nanopores, enhanced absorption in the wideband spectrum is achieved on the black silicon through the two-step etch process. Near-infrared light absorption has been found to improve using various surface treatments. Therefore, in this thesis, gold nanoparticles are used to generate a localized surface plasma effect to obtain better absorption performance than the black silicon samples without gold nanoparticles.

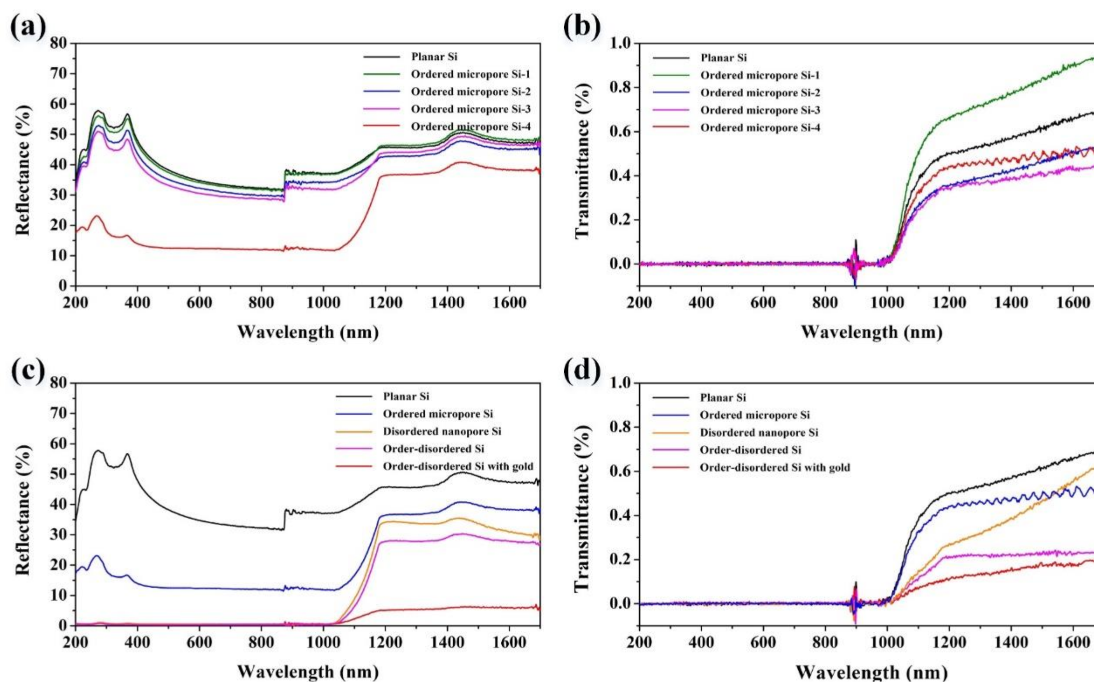

Figure 29 Optical measurements on silicon with different aperture to spacing ratios and etching processes. (a) The reflectance of planar silicon and honeycomb-like silicon with ordered micropores. (b) The transmittance of planar silicon and honeycomb-like silicon with ordered micropores. (c) The reflectance of silicon before and after different etching treatment steps. (d) The transmittance of silicon with different etching treatment steps. Ordered micropore sample Si-4 is chosen for the comparison tests in (c) and (d).

Figure 30 shows a photograph of samples fabricated with different etching parameters on a single wafer and their visual difference after different treatments. The square areas contain hierarchical surface texture consisting of honeycomb-like micropores and decorated nanopores. In contrast, the rest area on the wafer only contains nanopores.

The honeycomb-like black silicon with multiscale pores has a darker surface. This is a good example of how multiscale pores have a major effect on antireflection properties.

Figure 30 Digital photograph of a black silicon wafer in which the square areas contain hierarchical textures consisting of honeycomb-like micropores and decorated nanopores. In contrast, the remaining area contains only nanopores.

4.3 Light trapping via synergistic effect of hierarchical surface texture and LSPR particles with specific size

Recently, researchers have proposed femtosecond laser processing with chalcogenide to dope sulphur and oxygen into silicon materials to produce impurity levels in the silicon bandgap[46], [47], [63]. These impurities allow electrons to be excited across the bandgap by the absorption of two near-infrared photons, leading to a perfect trap of near-infrared light (NIR). However, it is difficult to control the distribution rate of each level and the amount of impurities. At the same time, these impurities require thermal annealing to realize dopant activation, which is high cost and time-consuming. Another notable approach is the use of metallic nanoparticles (NPs) to confine charge density oscillations and to induce localized surface plasmon resonance (LSPR)[33], [60]. Smaller NPs exhibit electromagnetic field enhancement under electromagnetic wave excitation, while light scattering dominates the optical response of larger NPs. Both effects contribute to the anti-reflective properties of black silicon. LSPR effects induced by

noble metals, alloys, different shapes, and mixed NPs have been applied on conventional anti-reflective surfaces. These strategies have proven to be highly successful for improving the overall anti-reflection performance of black silicon and the conversion efficiency of silicon-based photoelectronic devices. However, few studies take advantage of hierarchical surface textures decorated with LSPR particles to reduce surface reflectance further.

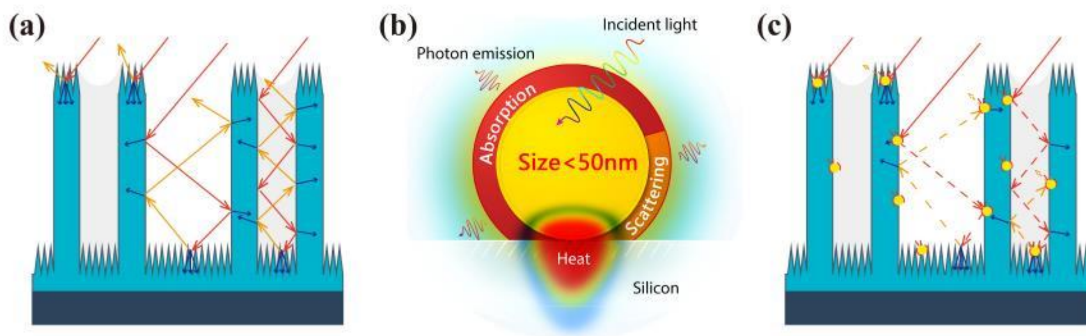

Figure 31 (a) Light trapping mechanism in black silicon with hierarchical texture. (b) Schematic diagram showing the dominant light absorption mechanism in Au NPs smaller than 50 nm. (c) Anti-reflection due to synergy between Au NP-induced LSPR and hierarchical texture of black silicon surface.

In this thesis, the as-fabricated chimney-like black silicon is selected to investigate light trapping via the synergistic effect of hierarchical surface texture and LSPR particles of a specific size. Light propagation plays an important role in studying the anti-reflection performance of black silicon with different textures.

In contrast to surface structures with micro or nano features, the hierarchical chimney-like surface texture offers large windows for the incident light. In addition, the vertical sidewalls guide the incoming light to reflecting inside along the depth direction. The reflected part reaches the bottom nanostructures and carries out diffuse reflection. These two behaviors can suppress the specular reflection on the top surface and increase diffuse reflection. On the surface texture of the hollow cylinder arrays, the nanopores on the top of the cylinders suppress the reflection loss of incident light. Mesopores and the spacing between hollow cylinders with larger sizes provide access for incoming optical waves. Their vertical walls allow incident light to be reflected in the

depth direction, providing more opportunities for light-material coupling. The reflected light along the sidewall diffusely reflects to the bottom decorated with nanopores. The diffuse reflection causes energy decay and optical path length extension as well as subsequent reflection along the sidewall. Therefore, the hierarchical surface structure takes advantage of both the micro and nanostructures. As depicted in Figure 31(a), this hierarchical texture design reduces specular reflection loss and facilitates the light-material coupling effect while extending the optical path length, resulting in ultralow reflection below 1100 nm.

Furthermore, metallic nanoparticle-induced LSPR is the key to addressing the challenge of high light reflection above 1100 nm. The electric field of optical waves covers metallic particles with sizes much smaller than the optical wavelength. This electric field polarizes conducting electrons in the metal lattice. When the frequency of incident light matches that of the valence electron oscillation, the incident light stimulates a collective resonance oscillation of the valence electrons in the solid, yielding electric dipoles. The restoring force between the electric dipoles impedes electron displacement, forming plasmon oscillations driven by resonant light waves. Only wavelengths resonant with these oscillations excite the LSPR. The photon energy injected into the plasmon oscillation produces attenuation through either radiative scattering or a non-radiative pathway. Radiative decay stems from the photon emission caused by electron-hole recombination and electron-phonon scattering, while non-radiative recombination causes the conversion of photons into heat. Photons can be scattered through several mechanisms in their travel, and there will be a deviation of band energies due to lattice vibrations. The relative effect of these two decay mechanisms determines the relative contributions from scattering and absorption. This balance changes with nanoparticle size, with increasing nanoparticle size enhancing radiative decay. According to Mie's theory regarding absorption and scattering in isolated Au NPs, the two effects are comparable when the size of the NPs is approximately 50 nm. The absorption prevails when the size of the NPs is less than 50 nm. The scattering phenomena on Au nanoparticles of roughly 20 nm account for only a few percent of total light attenuation. In particular, the light-to-heat conversion efficiency of particles with sizes above 2 nm

reaches 100%. Therefore, isolated Au NPs of less than 20 nm are likely the best candidate for transferring the energy of photons to black silicon. Figure 31(b) shows the dominant light absorption mechanism of Au nanoparticles smaller than 50 nm as well as the flow of thermal energy and heat carriers at the interface between a gold particle with LSPR and the bulk silicon. This investigation inspires us to explore the optimal configuration of Au NPs with LSPR on black silicon to further decrease reflectivity above 1100 nm through the dominant energy decay mechanism of thermal dissipation. For the first time, we have investigated the advantages of hierarchical structures and specific Au NPs to reduce reflectance from black silicon.

A synergistic effect is induced by light propagation through the hierarchical surface structures and energy decay in specific LSPR particles. Figure 31(c) shows the possible mechanism of this synergistic incident light trapping phenomenon. Light incident on the top surface is less likely to experience specular reflection due to metallic particle-induced photon absorption and scattering. The portion of light incident on the sidewalls is attenuated through plasmon oscillations on nanoparticles and silicon absorption. Reflected or scattered light is potentially further weakened on the other sidewalls through interactions with their surface metallic particles. The nanopores and nanoparticles at the bottom of the well collect remnant reflected and scattered light. Based on this analysis, it is expected that a broadband ultralow reflectivity can be achieved. Therefore, a systematic investigation of the synergy between hierarchical black silicon surface texture and Au NP-induced LSPR is crucial for upgrading the anti-reflectance properties of black silicon.

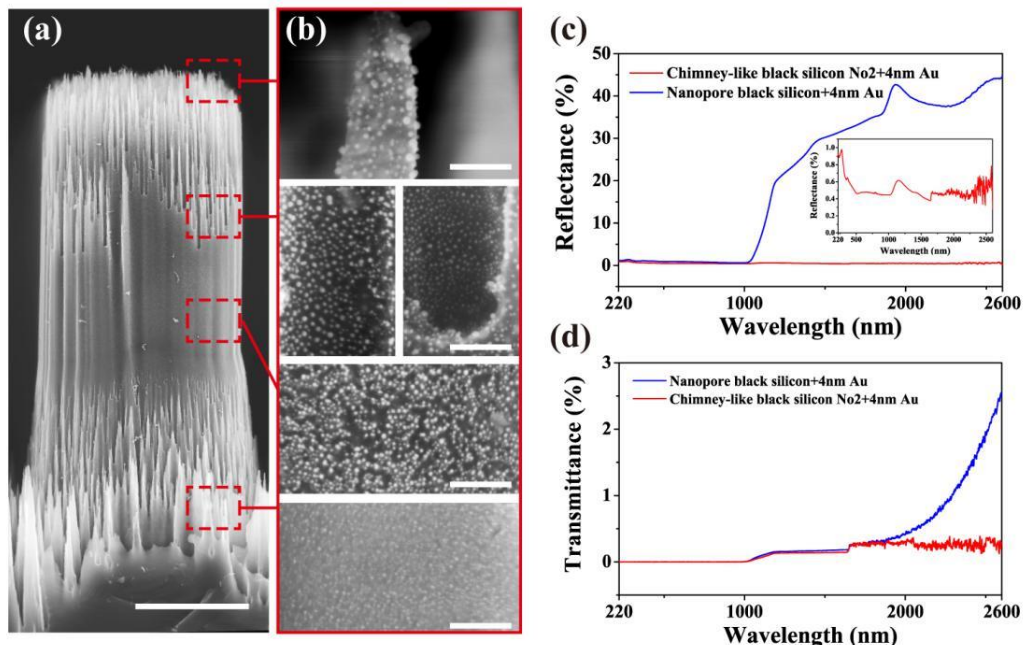

Figure 32 (a) Side view of the hierarchical chimney-like silicon structure decorated with Au NPs. The scale bar is 5 µm. (b) Magnified view of Au NPs at four selected positions on the hierarchal chimney-like silicon surface. All scale bars are 100 nm. (c) Measured reflectance spectra of the nanopore and hierarchical textured black silicon surfaces. Both structures are decorated with Au NPs formed from a 4 nm Au film. The inset shows a magnified view of the measured spectra from the hierarchical surface. (d) Measured transmittance spectra of the nanopore and hierarchical textured surface. Both are decorated with Au NPs formed from a 4 nm Au film.

Figure 32(a) shows an SEM image of the hierarchical chimney-like structure with Au NPs formed by the thermal annealing of a 4 nm gold film. As illustrated in Figure 32(b), the nanoparticles are observed on the upper pores, chimney sidewall, and bottom pores. The Au NPs in these regions have diverse sizes, spacing, and concentration, but they have a similar nanosphere shape. Their diameters are in the range of 5 to 20 nm, and the particles at the bottom are smaller than those in the upper region of the chimneys. This is because the three-dimensional structure causes the sputtered Au film to have a gradient thickness. The formed Au nanoparticles show a size difference after annealing, leading to an LSPR particle size gradient on the hierarchical surface. All the Au NPs are separate from each other with no visible agglomeration, and the spacing between adjacent particles is comparable to their size. These Au nanoparticles are strongly attached to the silicon surface due to the formation of metal-semiconductor bonds

during the thermal annealing processing, as shown in Figure S9. This process assists hot-spot formation and maximizes the number of particles. The widespread isolated Au NPs increase the occurrence of LSPR and increase the local-field trapping of a large number of photons. As shown in Figure 32(c), the reflectance spectrum of the hierarchal textured silicon surface presents a noticeable decrease in reflection compared to the silicon surface with only nanopores, which is aided by the nanoparticles deposited from the 4 nm gold film. The black silicon with a hierarchical structure provides an overall reflection of below 1.0% from 220 to 2600 nm. There are two possible reasons for the higher reflection of wavelengths above 1100 nm on the nanopore silicon surface. First, nanopores only provide limited windows to absorb incident infrared light, leading to inevitable reflection loss. Second, a smaller concentration of large Au particles on this surface leads to lower LSPR intensity. The inset image shows that the average reflectance of the chimney-like black silicon decorated with Au NPs is approximately 0.5% above 1100 nm, and the maximum reflectance of 0.6% occurs at 1250 nm. As shown in Figure 32(d), the overall transmittance of the chimney-like black silicon is less than 0.5% from 220 to 2600 nm. It is concluded that the energy decay occurring at the silicon/gold nanoparticle interface suppresses the reflection of infrared light and that the photons are most likely converted to heat. Thus, the hierarchical texture and Au NPs are responsible for the low broadband anti-reflectivity of the chimney-like black silicon.

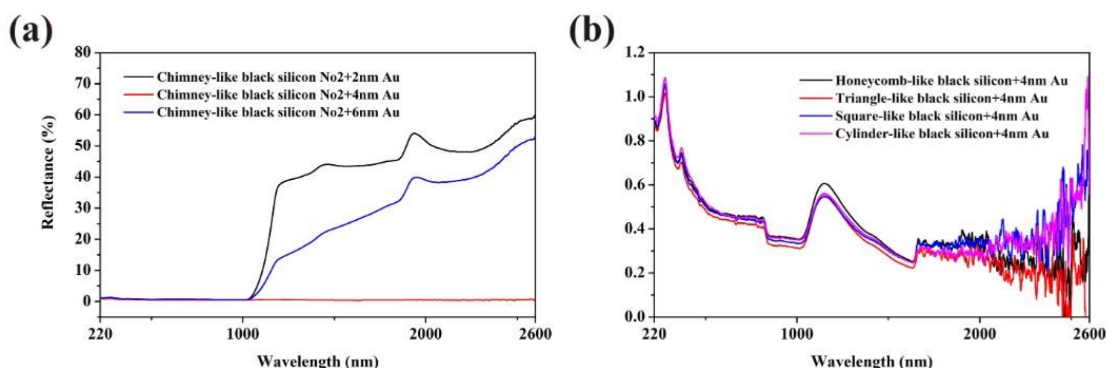

Figure 33 (a) Measured reflectance spectra of the hierarchical chimney-like black silicon decorated with nanoparticles formed from Au films with varying thickness. (b) Measured reflectance spectra of different hierarchical surface structures, all of which have the same nanopore decoration and Au NPs formed from a 4 nm gold film.

Au films with thicknesses of 2, 4, 6, 8, and 10 nm are fabricated to investigate the effect of particle size on reflection suppression. Thermal annealing at 500 °C for one hour is used to form the nanoparticles. Notably, the samples with nanoparticles formed by 8 and 10 nm gold films cannot have their reflectance spectra measured due to the appearance of an observable golden colour on their surfaces. Figure 33(a) shows that the black silicon decorated with nanoparticles formed by a 4 nm Au film has the lowest reflectance. In addition, the 6 nm film Au particles provide much lower reflectance than the 2 nm Au particles because the smaller particles in the 2 nm sample may cause relatively weak LSPR intensity. Figure 33(b) illustrates the measured reflection spectra of hierarchical texture designs with different micron structures (honeycomb, triangle, square, and cylinder) decorated with Au nanoparticles formed through 4 nm Au films. Their reflectance values are lower than 1% at the wavelength range from 220 to 2600 nm, evidencing that a 4 nm Au film creates the most effective Au particle.

4.4 Photo-thermal-electric generation

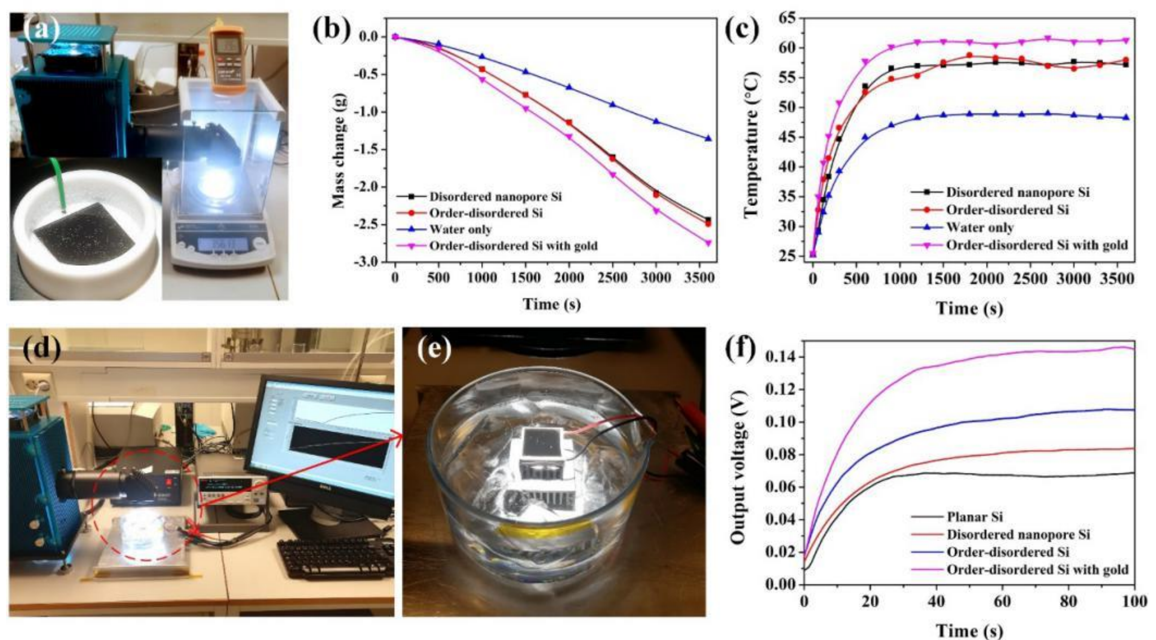

Figure 34 (a) Testing platform for steam generation. The inset photo shows the thermocouple detecting head immersed in water and bubble growth on the sample surface. (b) Change in the mass of water with time under 4 kW m^{-2} solar irradiation. (c) Water temperature vs. time. (d) Testing platform for photo-

thermal-electric experiment. A LabVIEW program was used to record real-time output. (e) The black silicon, generator, and cooling fin are fixed together using thermally conductive silicone and the aluminium fins are immersed in an ice-water mixture. (f) The output voltages of the thermoelectric generator vs. time. *Note: the order-disordered Si has honeycomb-like micropores and nanopores on its surface, and the disordered nanopore Si only has nanopores on its surface.*

Solar-driven evaporation and thermoelectric generation experiments are conducted to verify the light-trapping performance of the black silicon with hierarchical surface structures. Hierarchical honeycomb-like black silicon is tested as an illustration. First, bottom-heating-based evaporation is the first experiment. Black silicon absorbs light and converts it into thermal energy to heat 350 μL distilled water from the bottom of a vessel. As shown in Figure 34(a), a 22×22 mm^2 black silicon sample is fixed in a Teflon culture dish with a diameter of 40 mm and a depth of 13 mm. The low thermal conductivity of Teflon is crucial for reducing the impact of heat loss and heat exchange (conduction loss, upward convection with the surroundings, and radiation). A thermocouple-based thermometer is used to monitor the water temperature.

Figure 34(b) shows the mass change vs. illumination time due to steam generation. As is well-known, the efficient absorption of broadband solar radiation and its conversion into heat is crucial for driving liquid evaporation. After one hour of evaporation, the mass of the water is reduced by 1.35, 2.43, 2.50, and 2.73 g in trials with no silicon, nanopore silicon, micro-nanopore silicon, and micro-nanopore silicon with gold NPs, respectively. The evaporation rate of black silicon with Au NPs plasmon absorbers was about two times that of pure water and about 1.1 times that of other silicon samples in the experiment. The difference between the black silicon samples with nanopore and multiscale pores is not significant. This difference is potentially stemming from heat loss. Such heat loss inevitably occurs due to the separation of the heat source and the water surface and the temperature difference between them. Figure 34(c) shows the water temperature variation. The water temperature which initially increases and stabilizes in all four experiments. However, the increasing rates of the four samples are different. The black silicon with plasmon absorbers enables the fastest water heating and achieves the highest temperature of 62 °C. The performance of the order-disordered black silicon

with hierarchical texture design is very similar to that of disordered silicon. It is potentially explained by the heat loss error exceeding the performance difference. Therefore, a more sensitive testing approach is required to investigate the low variation between the micropore and micro-nanopore samples.

Silicon samples are attached to a commercial thermoelectric power generation module (TES1-4902) to be broadband light energy absorbers for the thermoelectric experiment. We investigated their photo-thermal-electric conversion properties systematically. The thermoelectric module has dimensions of 23×23 mm and a thickness of 3.9 mm. As shown in Figure 34(d), the module's cold side is joined to an aluminum radiator with cooling fins immersed into an ice-water mixture to obtain a constant temperature at the cold side. Black silicon is connected to the hot side with thermal silicone grease coating on its backside, as shown in Figure 34(e). A Keithley 2635B source meter and LabVIEW-control software are employed to measure the open-circuit voltage and study the real-time electrical output corresponding to the intrinsic absorption performance. The cold side is kept at a constant temperature, and the real-time signal acquisition system allows for a rapid and accurate response to the heat generated by black silicon. The thermal electric generator can record the minute temperature variations. Because once the trapped light energy is converted to heat, the temperature of the hot side increases. The resultant temperature difference between the cold and hot sides causes the generator's output voltage to fluctuate.

Figure 34(f) shows the four samples' initial voltage increase and saturation are different. The micro-nanopore silicon with Au NPs exhibits the highest output voltage of 140 mV. The micro-nanopore silicon without Au NPs shows a faster voltage change rate than the nanopore-only sample. And its maximum voltage is about 20 mV higher than the latter. The multiscale pore structures on black silicon enhance photothermal conversion. With a maximum voltage of 65 mV, planar silicon has the worst performance of all the samples examined. These results are consistent with the light trapping observations discussed in Section 4.2. As a result, micro-nanopore black silicon with hierarchical

texture design shows better photothermic conversion ability than nanopore black silicon.

4.5 Super-hydrophobicity on nanowire black silicon

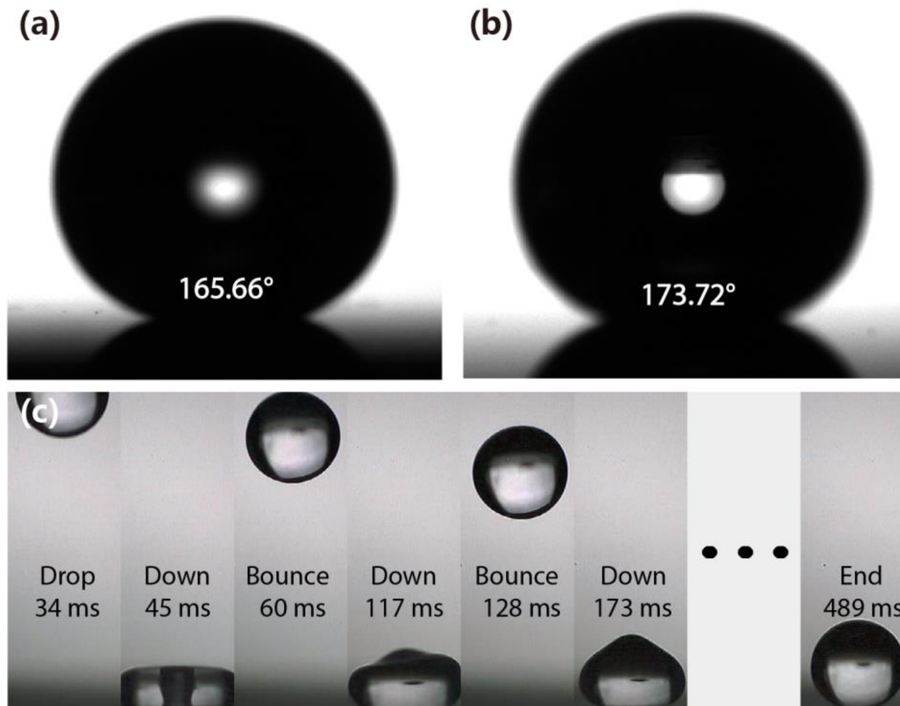

Figure 35 Contact angles of water droplets on nanowire black silicon surfaces formed through (a) 160 and (b) 180 etching loops. (c) Images of a 1.5 μL water droplet dropped onto a silicon nanowire surface bouncing ten times. The video framerate represents 4000 frames per second.

Silicon nanowires also possess unique structural properties. For example, one of the very different properties from bulk silicon is the remarkably enhanced surface hydrophobicity[64]–[66]. Meanwhile, hydrophobic characteristics are important in self-cleaning processes, antibacterial surfaces, and other biomedical applications. Octadecyl trichlorosilane (OTS) is often applied on hydrophobic surfaces as a chemical treatment to enhance structural hydrophobicity. However, such treatment may introduce contaminations and high costs. The OTS also suffers from poor long-term reliability. In this thesis, the as-fabricated silicon nanowire arrays exhibit extreme superhydrophobic behavior with contact angles higher than 165.6° without using the hydrophobic chemical treatment. The tested silicon nanowire array is formed by 160 modified Bosch etching

loops(Figure 35(a)). Figure 35(b) shows the contact angle of the silicon nanowire surface formed by a 4 nm Au film and 180 etching loops. This sample demonstrates an even higher water contact angle of 173.7°. In Figure 35(c), the selected frames from a high-speed video (4000 frames per second) record the overall process of a 1.5 µL water droplet dropping onto the nanowire surface from a height of 70 mm. Initially, the droplet shows a fully bouncing off from the surface. Subsequently, it bounces nine times again, and the vertex height decreases gradually, indicating a good surface superhydrophobicity. The reliability of superhydrophobicity of the silicon nanowire surface is evaluated by continuously dropping five thousand 20 µL water droplets from a height of 30 cm. There is no apparent damage to the nanowire surface, indicating good material stability.

5 Conclusions and future prospects

5.1 Conclusion

In this thesis, novel structural design and fabrication methodologies for black silicon have been investigated systematically, along with their optical properties. Besides, the as-prepared black silicon achieves excellent anti-reflection through the synergistic effect of hierarchical surface texture and LSPR-induced by Au NPs.

A two-step RIE method consisting of mask-assisted and maskless etching steps has been developed for the reliable fabrication of novel black silicon with hierarchical surface textures. The proposed two-step etching approach extends the optical path length of incident light. It facilitates the control over the fabrication process to yield specific spacing to aperture ratios and highly ordered surface textures. This approach helps overcome the limitations of the light-trapping ability of nanostructured black silicon and space-constrained shortcomings of subsequent material engineering. The systematic investigation of the structural parameters' influence on reflectance and transmittance reveals high broadband absorption on black silicon with vertical sidewalls and plasmon absorbers. Magnetron sputtering and thermal annealing deposited gold particles (diameters less than 20 nm) on the hierarchical surface texture to produce LSPR. The hierarchical surface texture increases the available particle deposition surface and yields particle size distribution gradient from the top of the textured surface to its bottom. As a result, the resulting plasmons generate the absorption-dominant effect on incident light other than light scattering. The synergy between the light trapping effect induced by surface structure and the absorption-dominant plasmon effect induced by Au nanoparticles yields ultralow reflectivity below 1% at wavelengths of 220-2600 nm on the fabricated black silicon with hierarchical surface texture.

A modified Bosch process has been developed to create silicon nanowires with high aspect ratios. The Au-nanoparticles formed by magnetron sputtering film and thermal annealing are used as the hard mask to achieve controllable structure densities. The resulting nanowire black silicon exhibites excellent anti-reflection performance, with a

reflectance value below 2% at the wavelength of 220 to 1100 nm. In addition, the Au NP-induced surface plasmons significantly enhanced such black silicon's near-unity anti-reflection, achieving a reflectance below 3% at wavelengths of 220 to 2600 nm. Interestingly, the nanowire black silicon array exhibits a superhydrophobic behaviour with a contact angle higher than 165.6° without using any hydrophobic chemical treatment. This behaviour allows water droplets to bounce off the superhydrophobic surface up to 10 times. The results above indicate that the nanowire black silicon is promising in photothermal, photocatalytic, supercapacitor, and microfluidic applications.

On the other hand, the published articles described in this thesis mainly focus on the fabrication and characterization of hierarchical black silicon. However, the creative methodology and results are significant to black silicon applications in optoelectronic, photocatalytic, photothermic, and microfluidic fields.

5.2 Future application

Black silicon is an emerging material with various surface structures and can achieve improved photodetection ability. In photodetectors, black silicon can significantly enhance the response sensitivity of photodetection from the visible to NIR wavelengths.[7], [67]–[70]. For instance, Schottky junction based on black silicon/Ag nanoparticles (Ag-NPs) can be applied in photodetection in the near-infrared regime[42]. This type of photodetector employs the synergistic mechanism of inner photoemission, light-trapping, and surface-plasmon-enhanced absorption. As a result, it can efficiently absorb the sub-bandgap photons and generate photocurrent.

At present, there are few research reports on black silicon-based UV photoelectric sensors. However, ultraviolet sensing is increasingly becoming important for many applications. UV sensing has multiple applications, including spectroscopy and imaging, flame detection, water purification and biotechnology. While annual market demand for UV photodiodes is expected to increase to 30%, the efficiency of these devices has

been limited to 80% at best. As a result, black silicon-based UV photodetection would be one of the future research focus.

5.2.1 Black-Silicon Ultraviolet Photodiodes with External Quantum Efficiency above 130%

Ultraviolet sensors have so far been utilized in various fields ranging from spectroscopy applications via biotechnical innovations to industrial process control. However, the performances of current ultraviolet sensors are still surprisingly poor. For instance, Aalto University researchers have developed a black silicon photodetector with efficiency above 130% (Figure 36(a)) [70]. The surface of black silicon is nanostructured with cones and columns that make the surface highly absorbent at all angles that light might be incident. Usually, using nanostructured surfaces to lower reflection leads to greater recombination so little net gain is made, but these devices were coated in Al_2O_3 to suppress this recombination [70]. The result is devices with not only near unity efficiency at wavelengths 250-950 nm, but efficiency exceeding 130% at 200 nm. SEM images of surface structures are shown in Figure 36(b) and 36(c). For the first time, a single photovoltaic device exceeding 100% external quantum efficiency limit is obtained under UV. This result opens new avenues for improving efficiencies beyond the famous Shockley-Queisser limit and inspire us to explore the ultraviolet photodetection on the novel black silicon with hierarchical surface textures.

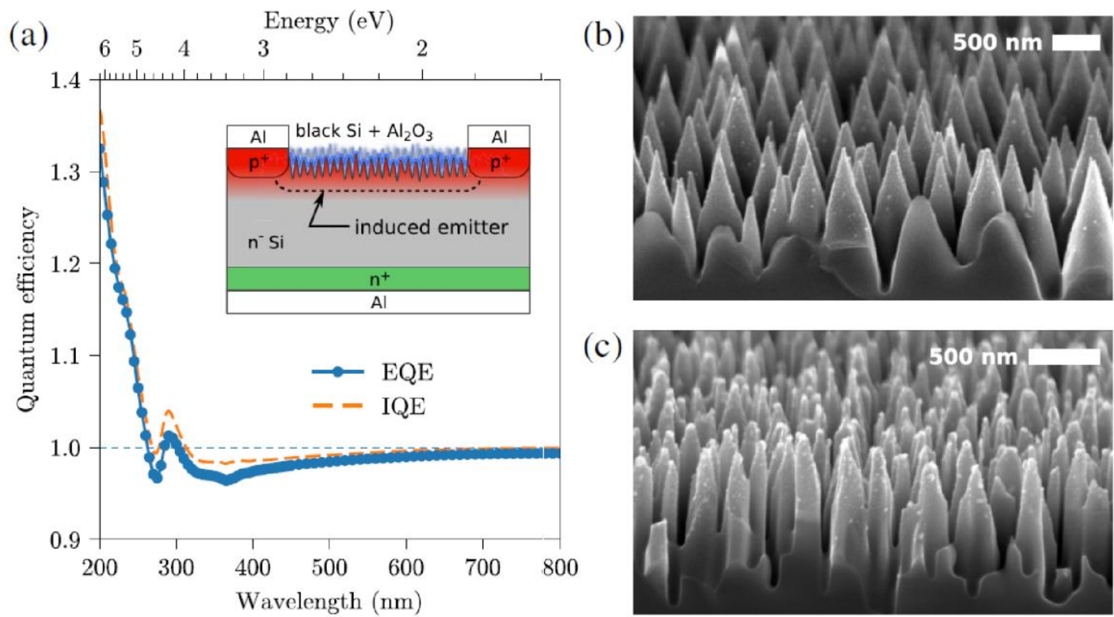

Figure 36 Black-Silicon Ultraviolet Photodiodes designed by researchers at Aalto University [70]. (a) A schematic diagram of photodiodes and quantum efficiency at wavelengths of 200 to 800 nm. SEM images of device structures. (b) and (c) Bird's eye view SEM image of b-Si nanotexture with cone-like and columnar-like morphologies, respectively.

5.2.2 Principle of black-silicon ultraviolet photodiodes

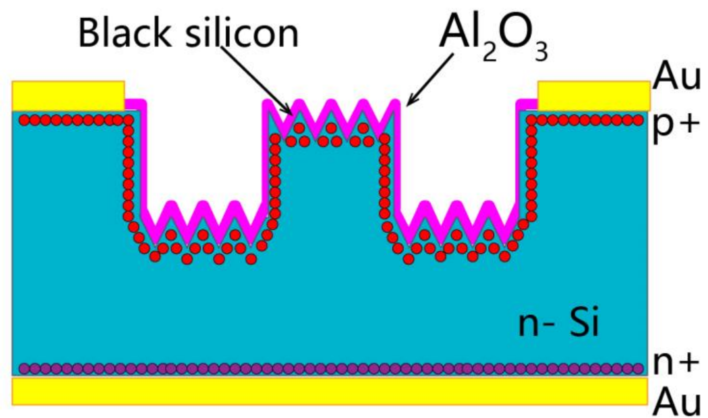

Figure 37 Cross-sectional view of our photodiode on the black silicon with hierarchical surface texture. (Unpublished)

A cross-section of the photodiode design on black silicon with hierarchical surface texture is illustrated in Figure 37. Alumina-coated micro-nanostructure is located on top of a high-resistivity n-type silicon substrate. Also, the presence of alumina induces an inversion layer in silicon, forming a depletion region. The gold is used as front and back electrodes. Below and above Au, boron (p+)- and phosphorus (n+)-implanted areas are formed to increase the quality of electronic contacts.

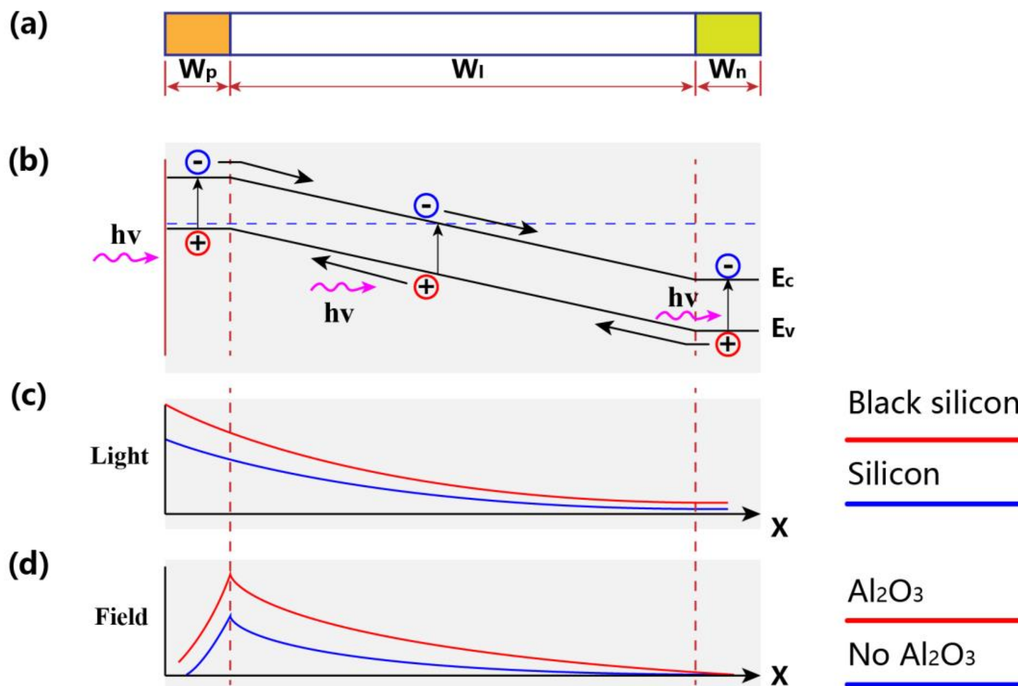

Figure 38 The working principle of the black silicon-based ultraviolet photodiode. (Unpublished)

The working principle of black silicon-based ultraviolet photodiode is depicted in Figure 38. At incident photon energy greater than or equal to material bandgap, the photons are absorbed by the substrate silicon, thereby exciting the valence band electrons in the positive, intrinsic, and negative regions to generate electron-hole pairs. Compared to ordinary silicon-based optoelectronic devices, the unique light-trapping ability on black silicon surfaces enhances the initial ultraviolet light absorption. This initial light absorption improvement, in turn, excites more electron-hole pairs and a self-built external electric field induced by the alumina film. Meanwhile, the film can enrich

electrons to generate an inversion layer in silicon, leading to the formation of a depletion region and a reverse bias voltage. The depletion region and bias voltage may accelerate the separation of electrons and holes, where electrons in the conduction band are accelerated to the n-zone. In contrast, the valence band holes are accelerated to the p-zone. These charge accelerations generate a higher photovoltage on the two electrodes of the device. As a result, a stronger photocurrent is formed in the circuit, meaning effective conversion of the received optical signal into an electrical signal at the output.

5.2.3 Fabrication process of Ultraviolet Photodiode on black silicon with hierarchical surface texture

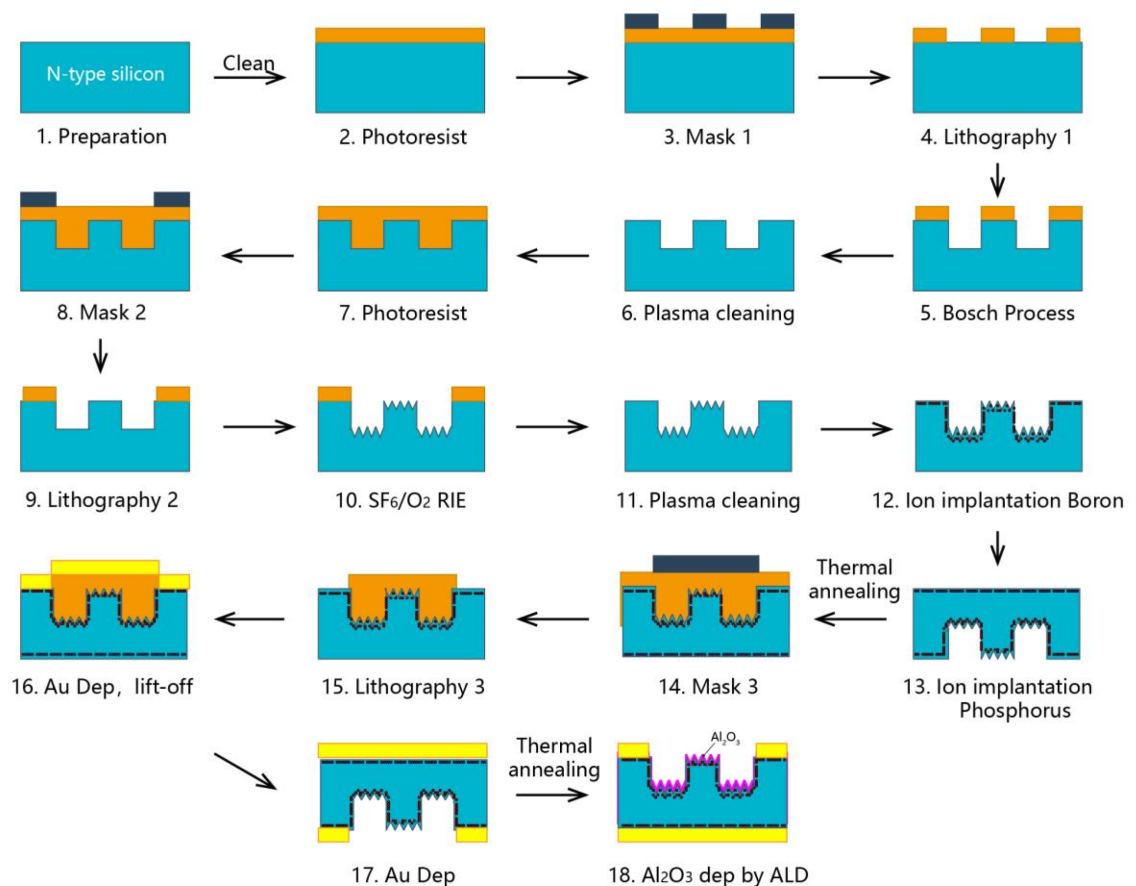

Figure 39 Fabrication process of ultraviolet photodiode on the black silicon with hierarchical surface texture. (Unpublished)

In this thesis, 500 µm thick high resistivity (>10 kΩ·cm) n-type 4-inch <100> oriented silicon wafers are used as substrate materials. Black silicon is formed on the active areas of the diodes by two-step RIE. The details of the fabrication process are provided in Figure 39. The black silicon region is surrounded by a boron-implanted area to realize an ohmic contact with the inversion layer. The active area is covered with ALD alumina, generating a negative charge in the inversion layer. Front and back metal contacts are formed by sputtering Au. The back side of the wafer is based on phosphorus-implanted to increase quality of the contact and formation of back-surface field. A digital photograph of black silicon ultraviolet photodiode on a 4-inch wafer is shown in Figure 40.

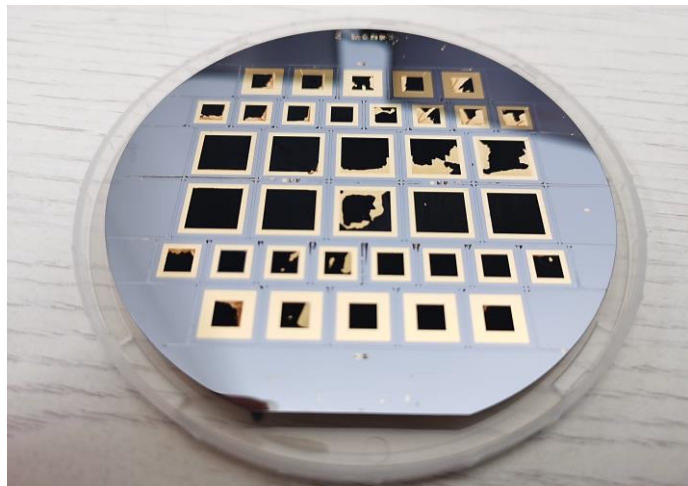

Figure 40 Digital photograph of black silicon ultraviolet photodiode on a 4-inch wafer. (Unpublished)

5.2.4 Future work

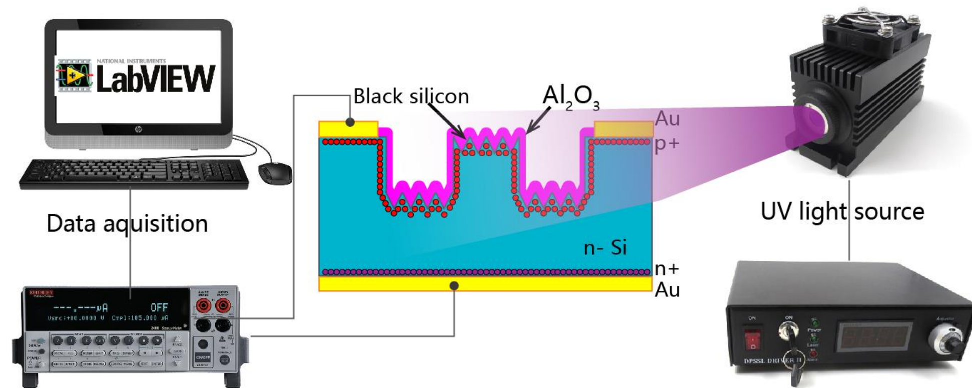

Figure 41 Testing platform. (Unpublished)

It is necessary to build a testing platform for the evaluation of as-made black silicon-based ultraviolet photodetector. The preliminary design of the real-time testing system is presented in Figure 41. It mainly consists of an UV light source, a source meter and a real-time software. The measurements of the current-voltage (I-V) and photocurrent are planned to test using a Keithley 2450 source meter and a lock-in amplifier (SR830).

Future work will focus on exploring the combination and create a better ultraviolet photodiode on novel black silicon with hierarchical surface textures, which will hopefully provide exciting results.

6 References

[1] J. Lv, T. Zhang, P. Zhang, Y. Zhao, and S. Li, "Review application of nanostructured black silicon," *Nanoscale Res. Lett.*, vol. 13, no. 1, 2018.

[2] C. Betty, "Porous Silicon: A Resourceful Material for Nanotechnology," *Recent Pat. Nanotechnol.*, vol. 2, no. 2, pp. 128–136, 2008.

[3] Z. Huang, N. Geyer, P. Werner, J. De Boor, and U. Gösele, "Metal-assisted chemical etching of silicon: A review," *Adv. Mater.*, vol. 23, no. 2, pp. 285–308, 2011.

[4] A. S. Mayer and B. C. Kirkpatrick, "Silicon photonics," *Front. Mod. Opt.*, vol. 24, no. 12, pp. 189–205, 2016.

[5] M. Otto *et al.*, "Black silicon photovoltaics," *Adv. Opt. Mater.*, vol. 3, no. 2, pp. 147–164, 2015.

[6] X. Liu, P. R. Coxon, M. Peters, B. Hoex, J. M. Cole, and D. J. Fray, "Black silicon: Fabrication methods, properties and solar energy applications," *Energy Environ. Sci.*, vol. 7, no. 10, pp. 3223–3263, 2014.

[7] F. Priolo, T. Gregorkiewicz, M. Galli, and T. F. Krauss, "Silicon nanostructures for photonics and photovoltaics," *Nat. Nanotechnol.*, vol. 9, no. 1, pp. 19–32, 2014.

[8] E. C. Garnett, M. L. Brongersma, Y. Cui, and M. D. McGehee, "Nanowire solar cells," *Annu. Rev. Mater. Res.*, vol. 41, pp. 269–295, 2011.

[9] E. Garnett and P. Yang, "Light trapping in silicon nanowire solar cells," *Nano Lett.*, vol. 10, no. 3, pp. 1082–1087, 2010.

[10] S. M. Thalluri *et al.*, "Highly-ordered silicon nanowire arrays for photoelectrochemical hydrogen evolution: An investigation on the effect of wire diameter, length and inter-wire spacing," *Sustain. Energy Fuels*, vol. 2, no. 5, pp. 978–982, 2018.

[11] X. Ao *et al.*, “Black silicon with controllable macropore array for enhanced photoelectrochemical performance,” *Appl. Phys. Lett.*, vol. 101, no. 11, pp. 3–6, 2012.

[12] R. Liu, T. Sun, J. Liu, S. Wu, and B. Sun, “Hybrid silicon honeycomb/organic solar cells with enhanced efficiency using surface etching,” *Nanotechnology*, vol. 27, no. 25, 2016.

[13] L. Baggetto, D. Danilov, and P. H. L. Notten, “Honeycomb-structured silicon: Remarkable morphological changes induced by electrochemical (De)lithiation,” *Adv. Mater.*, vol. 23, no. 13, pp. 1563–1566, 2011.

[14] T. Zhang, P. Zhang, S. Li, W. Li, Z. Wu, and Y. Jiang, “Black silicon with self-cleaning surface prepared by wetting processes,” *Nanoscale Res. Lett.*, vol. 8, no. 1, pp. 1–5, 2013.

[15] X. Ao *et al.*, “Black silicon with controllable macropore array for enhanced photoelectrochemical performance,” *Appl. Phys. Lett.*, vol. 101, no. 11, 2012.

[16] T. Chen, W. Wang, T. Tao, A. Pan, and X. Mei, “Multi-scale micro-nano structures prepared by laser cleaning assisted laser ablation for broadband ultralow reflectivity silicon surfaces in ambient air,” *Appl. Surf. Sci.*, vol. 509, no. September 2019, p. 145182, 2020.

[17] M. Baba, T. Jia, M. Suzuki, and H. Kuroda, “Femtosecond Laser Induced Nanowire Technique and Its Applications,” *ISRN Nanotechnol.*, vol. 2011, pp. 1–7, 2011.

[18] I. A. Buyanova, A. Henry, B. Monemar, J. L. Lindström, and G. S. Oehrlein, “Photoluminescence of defects induced in silicon by SF6/O 2 reactive-ion etching,” *J. Appl. Phys.*, vol. 78, no. 5, pp. 3348–3352, 1995.

[19] J. Müllerová, Ľ. Scholtz, J. Ďurišová, E. Pinčík, M. Solanská, and D. Pudiš, “Angle- and polarization resolved antireflection properties of black silicon prepared by

electrochemical etching supported by external electric field," *Appl. Surf. Sci.*, vol. 461, no. February, pp. 182–189, 2018.

[20] Y. Zhao *et al.*, "Oxidatively Stable Nanoporous Silicon Photocathodes with Enhanced Onset Voltage for Photoelectrochemical Proton Reduction," *Nano Lett.*, vol. 15, no. 4, pp. 2517–2525, 2015.

[21] J. Y. Li, C. H. Hung, and C. Y. Chen, "Hybrid black silicon solar cells textured with the interplay of copper-induced galvanic displacement," *Sci. Rep.*, vol. 7, no. 1, pp. 1–10, 2017.

[22] F. Toor *et al.*, "Metal assisted catalyzed etched (MACE) black Si: Optics and device physics," *Nanoscale*, vol. 8, no. 34, pp. 15448–15466, 2016.

[23] H. Jansen, M. De Boer, R. Legtenberg, and M. Elwenspoek, "The black silicon method: A universal method for determining the parameter setting of a fluorine-based reactive ion etcher in deep silicon trench etching with profile control," *J. Micromechanics Microengineering*, vol. 5, no. 2, pp. 115–120, 1995.

[24] F. Alexander *et al.*, "Water splitting TiO2 composite material based on black silicon as an efficient photocatalyst," *Sol. Energy Mater. Sol. Cells*, vol. 180, no. May 2017, pp. 236–242, 2018.

[25] Y. Yu *et al.*, "Enhanced photoelectrochemical efficiency and stability using a conformal TiO2 film on a black silicon photoanode," *Nat. Energy*, vol. 2, no. 6, 2017.

[26] M. Gaidi, K. Daoudi, S. Columbus, A. Hajjaji, M. A. El Khakani, and B. Bessais, "Enhanced photocatalytic activities of silicon nanowires/graphene oxide nanocomposite: Effect of etching parameters," *J. Environ. Sci. (China)*, vol. 101, pp. 123–134, 2021.

[27] C. H. Tang, P. H. Hsiao, and C. Y. Chen, "Efficient Photocatalysts Made by Uniform Decoration of Cu2O Nanoparticles on Si Nanowire Arrays with Low Visible Reflectivity," *Nanoscale Res. Lett.*, vol. 13, 2018.

[28] Y. Liu, G. Ji, J. Wang, X. Liang, Z. Zuo, and Y. Shi, "Fabrication and photocatalytic properties of silicon nanowires by metal-assisted chemical etching: Effect of H2O2 concentration," *Nanoscale Res. Lett.*, vol. 7, no. 1, pp. 1–9, 2012.

[29] D. Liu, L. Li, Y. Gao, C. Wang, J. Jiang, and Y. Xiong, "The nature of photocatalytic 'water splitting' on silicon nanowires," *Angew. Chemie - Int. Ed.*, vol. 54, no. 10, pp. 2980–2985, 2015.

[30] A. Furube and S. Hashimoto, "Insight into plasmonic hot-electron transfer and plasmon molecular drive: new dimensions in energy conversion and nanofabrication," *NPG Asia Mater.*, vol. 9, no. 12, p. e454, 2017.

[31] C. Ye, L. Zhang, X. Fang, Y. Wang, P. Yan, and J. Zhao, "Hierarchical structure: Silicon nanowires standing on silica microwires," *Adv. Mater.*, vol. 16, no. 12, pp. 1019–1023, 2004.

[32] Z. Yue, H. Shen, and Y. Jiang, "Antireflective nanostructures fabricated by reactive ion etching method on pyramid-structured silicon surface," *Appl. Surf. Sci.*, vol. 271, pp. 402–406, 2013.

[33] J. Yang *et al.*, "Design and fabrication of broadband ultralow reflectivity black Si surfaces by laser micro/nanoprocessing," *Light Sci. Appl.*, vol. 3, no. 000, p. 0, 2014.

[34] H. Zhong, N. Ilyas, Y. Song, W. Li, and Y. Jiang, "Enhanced near-infrared absorber: two-step fabricated structured black silicon and its device application," *Nanoscale Res. Lett.*, vol. 13, 2018.

[35] B. Zheng, W. Wang, G. Jiang, and X. Mei, "Fabrication of broadband antireflective black metal surfaces with ultra-light-trapping structures by picosecond laser

texturing and chemical fluorination," *Appl. Phys. B Lasers Opt.*, vol. 122, no. 6, pp. 1–15, 2016.

[36] G. Sun, T. Gao, X. Zhao, and H. Zhang, "Fabrication of micro/nano dual-scale structures by improved deep reactive ion etching," *J. Micromechanics Microengineering*, vol. 20, no. 7, 2010.

[37] Z. Fan *et al.*, "Recent progress of black silicon: From fabrications to applications," *Nanomaterials*, vol. 11, no. 1, pp. 1–26, 2021.

[38] M. Stubenrauch, M. Fischer, C. Kremin, S. Stoebenau, A. Albrecht, and O. Nagel, "Black silicon—new functionalities in microsystems," *J. Micromechanics Microengineering*, vol. 16, no. 6, pp. S82–S87, 2006.

[39] C. H. Choi and C. J. Kim, "Fabrication of a dense array of tall nanostructures over a large sample area with sidewall profile and tip sharpness control," *Nanotechnology*, vol. 17, no. 21, pp. 5326–5333, 2006.

[40] H. Savin *et al.*, "Black silicon solar cells with interdigitated back-contacts achieve 22.1% efficiency," *Nat. Nanotechnol.*, vol. 10, no. 7, pp. 624–628, 2015.

[41] P. Hoyer, M. Theuer, R. Beigang, and E. B. Kley, "Terahertz emission from black silicon," *Appl. Phys. Lett.*, vol. 93, no. 9, 2008.

[42] F. Hu *et al.*, "Black silicon Schottky photodetector in sub-bandgap near-infrared regime," *Opt. Express*, vol. 27, no. 3, p. 3161, 2019.

[43] Q. Tan, F. Lu, C. Xue, W. Zhang, L. Lin, and J. Xiong, "Nano-fabrication methods and novel applications of black silicon," *Sensors Actuators, A Phys.*, vol. 295, pp. 560–573, 2019.

[44] Z. Zhang *et al.*, "Ultralow Broadband Reflectivity in Black Silicon via Synergy between Hierarchical Texture and Specific-Size Au Nanoparticles," *Adv. Opt. Mater.*, vol. 8, no. 19, 2020.

[45] Z. Zhang *et al.*, “Black silicon with order-disordered structures for enhanced light trapping and photothermic conversion,” *Nano Energy*, vol. 65, no. June, p. 103992, 2019.

[46] A. Y. Vorobyev and C. Guo, “Direct creation of black silicon using femtosecond laser pulses,” *Appl. Surf. Sci.*, vol. 257, no. 16, pp. 7291–7294, 2011.

[47] S. Kontermann, T. Gimpel, A. L. Baumann, K. M. Guenther, and W. Schade, “Laser processed black silicon for photovoltaic applications,” *Energy Procedia*, vol. 27, no. May 2014, pp. 390–395, 2012.

[48] J. M. Duran and A. Sarangan, “Fabrication of ultrahigh aspect ratio silicon nanostructures using self-assembled gold metal-assisted chemical etching,” *J. Micro/Nanolithography, MEMS, MOEMS*, vol. 16, no. 1, p. 014502, 2017.

[49] Z. R. Chowdhury, J. Y. Y. Loh, M. N. N. Pishon, and N. P. Kherani, “Black silicon morphologies using conventional RIE processing,” *AIP Adv.*, vol. 7, no. 5, pp. 1–8, 2017.

[50] H. V. Jansen, M. J. De Boer, S. Unnikrishnan, M. C. Louwerse, and M. C. Elwenspoek, “Black silicon method X: A review on high speed and selective plasma etching of silicon with profile control: An in-depth comparison between Bosch and cryostat DRIE processes as a roadmap to next generation equipment,” *J. Micromechanics Microengineering*, vol. 19, no. 3, 2009.

[51] K. Kim, J. K. Lee, S. J. Han, and S. Lee, “A novel top-down fabrication process for vertically-stacked silicon-nanowire array,” *Appl. Sci.*, vol. 10, no. 3, 2020.

[52] F. Laermer and A. Urban, “MEMS at Bosch – Si plasma etch success story, history, applications, and products,” *Plasma Process. Polym.*, vol. 16, no. 9, pp. 1–12, 2019.

[53] P. Lin, X. Xie, Y. Wang, B. Lian, and G. Zhang, “A multi-step etch method for fabricating slightly tapered through-silicon vias based on modified Bosch process,” *Microsyst. Technol.*, vol. 25, no. 7, pp. 2693–2698, 2019.

[54] C. K. Chung, H. C. Lu, and T. H. Jaw, “High aspect ratio silicon trench fabrication by inductively coupled plasma,” *Microsyst. Technol.*, vol. 6, no. 3, pp. 106–108, 2000.

[55] M. Boufnichel, S. Aachboun, F. Grangeon, P. Lefaucheux, and P. Ranson, “Profile control of high aspect ratio trenches of silicon. I. Effect of process parameters on local bowing,” *J. Vac. Sci. Technol. B Microelectron. Nanom. Struct.*, vol. 20, no. 4, p. 1508, 2002.

[56] T. T. Bui, H. P. Tu, and M. C. Dang, “DRIE process optimization to fabricate vertical silicon nanowires using gold nanoparticles as masks,” *Adv. Nat. Sci. Nanosci. Nanotechnol.*, vol. 6, no. 4, p. 45016, 2015.

[57] S. C. Chen, C. Y. Kuo, Y. C. Lin, J. C. Wu, and L. Horng, “Parameter investigation of nano-sized etching in an ICP silicon etching system,” *NanoSingapore 2006 IEEE Conf. Emerg. Technol. - Nanoelectron. - Proc.*, vol. 2006, no. February, pp. 467–471, 2006.

[58] Y. Xia, B. Liu, S. Zhong, and C. Li, “X-ray photoelectron spectroscopic studies of black silicon for solar cell,” *J. Electron Spectros. Relat. Phenomena*, vol. 184, no. 11–12, pp. 589–592, 2012.

[59] X. Liu, J. Gao, and H. Yang, “Broadband near-infrared absorption enhancement in Si substrate via random distributed Ag nanoparticles,” *J. Mater. Sci. Mater. Electron.*, vol. 27, no. 10, pp. 10479–10483, 2016.

[60] S. Kessentini *et al.*, “Gold dimer nanoantenna with slanted gap for tunable LSPR and improved SERS,” *J. Phys. Chem. C*, vol. 118, no. 6, pp. 3209–3219, 2014.

[61] J. Flick, N. Rivera, and P. Narang, “Strong light-matter coupling in quantum chemistry and quantum photonics,” *Nanophotonics*, vol. 7, no. 9, pp. 1479–1501, 2018.

[62] J. Cai and L. Qi, “Recent advances in antireflective surfaces based on nanostructure arrays,” *Mater. Horizons*, vol. 2, no. 1, pp. 37–53, 2015.

[63] T. H. Her, R. J. Finlay, C. Wu, S. Deliwala, and E. Mazur, “Microstructuring of silicon with femtosecond laser pulses,” *Appl. Phys. Lett.*, vol. 73, no. 12, pp. 1673–1675, 1998.

[64] T. M. Schutzius, S. Jung, T. Maitra, G. Graeber, M. Köhme, and D. Poulikakos, “Spontaneous droplet trampolining on rigid superhydrophobic surfaces,” *Nature*, vol. 527, no. 7576, pp. 82–85, 2015.

[65] “STrongly superhydrophobicity silicon nanowires by supercritical CO2 drying.pdf.”

[66] C. Hao *et al.*, “Superhydrophobic-like tunable droplet bouncing on slippery liquid interfaces,” *Nat. Commun.*, vol. 6, pp. 1–7, 2015.

[67] M. A. Juntunen, J. Heinonen, V. Vähänissi, P. Repo, D. Valluru, and H. Savin, “Near-unity quantum efficiency of broadband black silicon photodiodes with an induced junction,” *Nat. Photonics*, vol. 10, no. 12, pp. 777–781, 2016.

[68] M. U. Pralle *et al.*, “Black silicon enhanced photodetectors: a path to IR CMOS,” *Infrared Technol. Appl. XXXVI*, vol. 7660, no. May 2010, p. 76600N, 2010.

[69] Z. Qi *et al.*, “Au nanoparticle-decorated silicon pyramids for plasmon-enhanced hot electron near-infrared photodetection,” *Nanotechnology*, vol. 28, no. 27, 2017.

[70] M. Garin *et al.*, “Black-Silicon Ultraviolet Photodiodes Achieve External Quantum Efficiency above 130%,” *Phys. Rev. Lett.*, vol. 125, no. 11, pp. 1–7, 2020.

7 Articles

Article 1

Z. Zhang et al., “Black silicon with order-disordered structures for enhanced light trapping and photothermic conversion,” Nano Energy, vol. 65, no. June, p. 103992, 2019, doi: 10.1016/j.nanoen.2019.103992

Article 2

Z. Zhang et al., “Ultralow Broadband Reflectivity in Black Silicon via Synergy between Hierarchical Texture and Specific-Size Au Nanoparticles,” Adv. Opt. Mater., vol. 8, no. 19, 2020, doi: 10.1002/adom.202000668

Article 3

Z. Zhang et al., “Fabrication of needle-like silicon nanowires by using a nanoparticles-assisted Bosch process for both high hydrophobicity and anti-reflection,” Micromachines. https://doi.org/10.3390/mi12091009.

Article 4

Z. Zhang, K. Du, X. Chen, C. Xue, and K. Wang, “An air-cushion triboelectric nanogenerator integrated with stretchable electrode for human-motion energy harvesting and monitoring,” Nano Energy, vol. 53, no. June, pp. 108–115, 2018, doi: 10.1016/j.nanoen.2018.08.011 ***(Not included in this thesis)***

Doctoral dissertation no. 116
2022

—

Hierarchical Black Silicon and Their Applications
Dissertation for the degree of PhD

—

Zengxing Zhang

—

ISBN 978-82-7206-635-1 (print)
ISBN 978-82-7206-636-8 (online)

usn.no